Continuum Mech. Thermodyn. (2019) 31:1339–1367
https://doi.org/10.1007/s00161-019-00746-6

ORIGINAL ARTICLE

Zineeddine Louna · Ibrahim Goda · Jean-François Ganghoffer

Homogenized strain gradient remodeling model for trabecular bone microstructures

Received: 28 September 2018 / Accepted: 18 January 2019 / Published online: 13 February 2019

Abstract Constitutive models for bone remodeling are established from micromechanical analyses at the scale of individual trabeculae defining the representative unit cell (RUC), accounting for both first- and second-order deformation gradients. On the microscale, trabeculae undergo apposition of new bone modeled by a surface growth velocity field driven by a mechanical stimulus identified to the surface divergence of an Eshelby-like tensor. The static and evolutive first and second gradient effective properties of a periodic network of bone trabeculae are evaluated by numerical simulations with controlled imposed first and second displacement gradient rates over the RUC. The formulated effective growth constitutive law at the scale of the homogenized set of trabeculae relates the (average) first and second growth strain rates to the homogenized stress and hyperstress tensors. The constitutive model is identified relying on the framework of TIP (thermodynamics of irreversible processes), adopting a split of the kinematic and static tensors into their deviator and hydrostatic contributions. The obtained results quantify the strength and importance of strain gradient effects on the overall remodeling process.

Keywords External and internal remodeling · Trabecular bone · Surface growth · Homogenized strain gradient growth model · Micromechanics

1 Introduction

The focus of this work is the setting up of a modeling framework accounting for both first- and second-order deformation gradients, relying on the thermodynamics of surfaces and configurational forces for the simulations of the evolution of the external bone surface induced by mechanical stimulations. We would in particular show that strain gradient model allows for the description of microstructure-related size effects which are known to be important in hierarchically heterogeneous materials like trabecular bones.

Communicated by Andreas Öchsner.

Z. Louna
LMFTA, Faculté de physique, USTHB, BP 32, El Alia, 16111 Bab Ezzouar Algiers, Algeria

I. Goda
LPMT, Université de Haute-Alsace, 11 rue Alfred Werner, 68093 Mulhouse Cedex, France

I. Goda
Department of Industrial Engineering, Faculty of Engineering, Fayoum University, Fayoum 63514, Egypt

J. Ganghoffer (✉)
CNRS, LEM3– Université de Lorraine, 7, rue Félix Savart, 57073 Metz, France
E-mail: jean-francois.Ganghoffer@univ-lorraine.fr

Bone continuously adjusts its mass, architecture, and properties to variations in its mechanical environment, a process coined bone remodeling and encompassing two recognized distinct mechanisms deserving the names internal and external remodeling [8]. Internal remodeling is associated with the resorption or reinforcement of bone material internally, accompanied by the removal and densification of cancellous bone architecture, without, however, changing the bone overall shape. Opposite to this, external or surface remodeling refers to the resorption or apposition of new bone material on the external bone surface, resulting in a change of the external shape of the overall bone structure. These processes strongly influence the overall behavior and health of the entire body; thus, the ability to perform bone remodeling simulations is of great importance. Such a need for the setting up of computational models of bone remodeling is particularly obvious in applications dealing with bone adaptivity, like bone implants and scaffold design (e.g., [13,45]), and furthermore to predict the outcome of dental or orthodontic treatment, as explained in [14,49].

A clear classification underlying bone change of mass (growth) can be made between volumetric and surface growth, as underlined in [11,19,25,46]. Volumetric growth takes place in the bulk of the material (occurring essentially for soft biological tissues), while surface growth is associated with the mechanisms underlying deposition of mass at a surface, mostly occurring in hard tissues. Epstein [10] lends, however, to think that the distinction between volumetric and surface growth is not so marked, at least from a kinetic point of view, as the two mechanisms may simply be two facets of the same reality. A unified vision of volumetric and surface growth has been brought more recently in Ganghoffer and Sokolowski [19], based on a micromechanical view of the growth of tissue elements within a host matrix. Furthermore, Ciarletta et al. [6] developed a unified thermomechanical theory for coupling bulk and surface growth processes with mass transport phenomena across boundaries and/or material interfaces.

Important size effects are known concerning the elastic behavior of single osteons [32], cortical bone [5,15,42,49,50], and trabecular bone [21,22,26,27,29,43]. For single osteon, the size effects are attributed to the compliance of the interfaces separating the laminae. As to trabecular bone, there exists experimental evidence that the cement lines considered as compliant interfaces account for most of the difference in stiffness between osteons and the entire bone. If continuum properties vary by more than 20–30% over a distance spanning three to five trabeculae, a continuum model for the structure is suspect as reported in Harrigan et al. [29]. Although many continuum models of trabecular bone have been developed over the last two decades under the umbrella of classical elasticity (e.g., [4,47]), those models indeed ignore microstructure-related scale effects on the macroscopic mechanical properties. They accordingly do not provide a satisfactory description of the bone behavior when the microstructural size of bone is comparable to the macroscopic length scale. The main idea promoted in this work is to incorporate such size effects and microstructural phenomena by employing a strain gradient continuum theory to describe the evolutive bone microstructure.

The structural hierarchy of materials with microstructures such as trabecular bones plays an important role in determining their macroscopic mechanical behavior as well as the stress and strain distribution at the macroscopic scale. Such microstructural effects become especially pronounced in the vicinity of the bone–implant interfaces and more generally in zones witnessing high strain gradients. This issue can be investigated using generalized continuum mechanics theories for bones known to be a heterogeneous material with microstructural features. A number of phenomenological remedies to the lack of microstructural features (like internal lengths parameters) of Cauchy (first gradient) elasticity have been proposed in the past decades requiring to abandon the local action hypothesis of classical continuum mechanics. Such enriched continuum models aim at incorporating microstructural information, and they follow three possible main strategies: (1) non-local integral models [12,30]; (2) higher-order gradient models [1,3,9,20,24,36,37,44]; and (3) Cosserat theories and variants of it, like Koiter model [2,7,21,23].

It is then natural to extend the strain gradient model of the static continuum properties of trabecular bone to the description of the evolutionary aspects associated with bone remodeling. This is further motivated from a biological point of view by the fact that osteocytes sense a mechanical signal based on the strain energy density, which itself includes strain gradient terms. One may nevertheless underline that strain gradient effects may become pronounced at the level of the osteocytes network when the internal strain gradient lengths are comparable to the average distance between osteocytes.

A continuum mixture theory with strain gradient terms has been developed recently in Madeo et al. [36] and extended later on to a visco-poro-elastic model applicable to bio-resorbable grafts [20], whereby the evolutionary equations for the internal bone density depend on the strain energy density (itself accounting for strain gradient terms). This model is phenomenological, and thus, it motivates for the setting up of micromechanical schemes built at the finer scale of a set of trabeculae to formulate such bone growth models.

The continuum gradient enhanced models employed in this work will be accordingly richer than standard Cauchy continuum, including higher gradients of displacement in the deformation energy, arising from the introduction of more complicated contact actions depending, e.g., on the curvature of the Cauchy cut (so-called double forces). The additional terms in the energy involving second gradient of the displacement arise from the consideration of the geometry of the trabecular architecture. Trabecular bone struts are indeed organized as a lattice structure oriented along the principal stress directions; this entails that the amount of deformation energy stored in bending of the trabeculae has to be considered. Thus, classical first gradient theories are not rich enough and new energy contributions describing the curvature of the trabecular microstructure have to be considered which naturally leads to strain gradient models.

The main novelty advocated in the present paper is to construct constitutive models for bone remodeling relying on micromechanical analyses at the scale of a representative volume element of trabecular bone structure, accounting for both first- and second-order deformation gradients. The static and evolutive homogenized properties of a periodic network of bone trabeculae shall be evaluated by combining a methodology for the evaluation of the average kinematic and static variables over a trabecular unit cell and numerical simulations with controlled imposed first and second strain rates. The use of a strain gradient model does explicitly allow accounting for the precise microstructure of the porous trabecular network, i.e., for the geometric distribution of porosity and the size of the pores inside the RVE. Notwithstanding, an averaged evolutive response is accounted for in this model and a precise constitutive form for this parameter in terms of the apparent density of the constituents is given. In order to explicitly take into account the precise porosity patterns of the trabecular bone structure, some numerical homogenization procedures will be used of the type presented in Goda and Ganghoffer [24]. The constitutive model is next identified relying on the framework of thermodynamics of irreversible processes, adopting a split of the kinematic and static tensors into their deviator and hydrostatic contributions. The formulated effective growth constitutive law at the scale of the homogenized set of trabeculae therefor relates the average first and second growth strain rates to the homogenized stress and hyperstress tensors, weighted by a nonlinear function of the evolving apparent density.

The outline of the paper is as follows: The average kinematics of the strain gradient continuum is elaborated in Sect. 2. The surface growth kinetics is formulated in Sect. 3 in terms of a relation between the surface growth velocity and a suitable driving force. A strain gradient bone remodeling theory is exposed in Sect. 4, relying on a micromechanical analysis performed over 2D sections of 3D real trabecular bone samples. The determination of the homogenized first and second gradient stiffness tensors for the initial and grown trabecular bone is done in Sect. 5. A strain gradient remodeling constitutive law for trabecular bone is identified in the framework of the thermodynamics of irreversible processes and relying on virtual tests in Sect. 6. We conclude in Sect. 7 by a summary of the present work and ideas for future developments.

2 Homogenized kinematics: effective volumetric growth and elastic tensors

We consider a domain consisting of a growing phase of trabecular bone skeleton in a surrounding matrix phase (typically the marrow phase). To describe the average kinematics of this domain at the mesoscale, we denote V the volume of the overall domain, and V_B, V_M, respectively, the volume of the domains occupied by the bone tissue and surrounding matrix.

Nowadays image-based meshing offers interesting opportunities based on microstructures scan data to computational continuum micromechanics methods for material characterization [28,38,40]. This approach turns out to be very attractive in materials science where the link between macroscopic properties and the microstructure of a material is sought. The high-resolution micro-computed tomography (μCT) has become a standard and essential tool for the measurement and visualization of bone structure. Imaging is performed on femoral neck trabecular bone at a nominal voxel size of 8.8 μm. 3D μCT scan data of cubic sample (9.97 mm/side) are obtained, and the data are straightforwardly segmented using threshold and flood fill tools in Simpleware's ScanIP software, as exposed in Fig. 1a. The bone microstructures are based on real 3D images of trabecular bone, from which a 2D section has been obtained (Fig. 1b).

We next describe the main elements toward the elaboration the first and second gradient average kinematics for the two-phase domain of the trabecular bone sample.

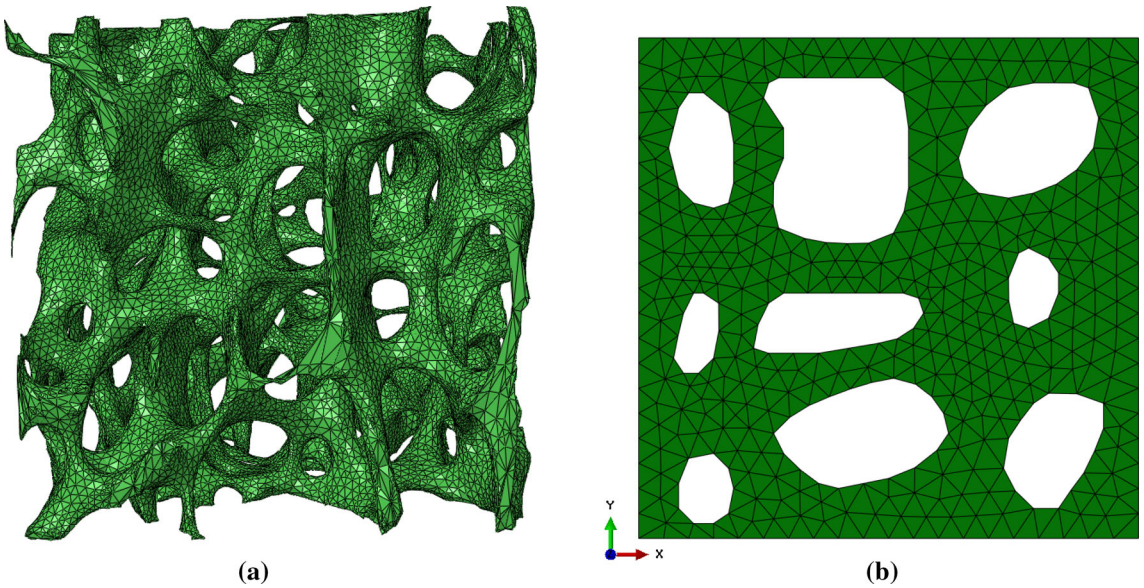

(a) **(b)**

Fig. 1 **a** 3D trabecular bone sample and **b** 2D section

2.1 First and second gradient average kinematics and statics

The Cauchy stress and hyperstress tensors can be constructed based on the extension of Hill–Mandel equivalence principle, viz.

$$\langle \boldsymbol{\sigma} : \dot{\boldsymbol{\varepsilon}} \rangle = \langle \boldsymbol{\sigma} \rangle : \langle \dot{\boldsymbol{\varepsilon}} \rangle + \langle \boldsymbol{\sigma} \otimes \mathbf{x} \rangle \dot{\mathbf{K}} \rightarrow \boldsymbol{\Sigma} := \langle \boldsymbol{\sigma} \rangle \, , \boldsymbol{\Sigma}^{\mathbf{S}} := \langle \boldsymbol{\sigma} \otimes \mathbf{x} \rangle \tag{2.1}$$

which successively defines the effective Cauchy stress and hyperstress tensors and the second- and third-order tensors $\boldsymbol{\Sigma}$, $\boldsymbol{\Sigma}^{\mathbf{S}}$, respectively. This writing also provides the average kinematics in terms of the average displacement, the linearized displacement gradient, and the strain gradient tensor, successively given by

$$\begin{aligned} &\mathbf{U}(\mathbf{X}) := \langle \boldsymbol{u}(\mathbf{x}) \rangle_{\mathrm{V}(\mathbf{X})} \, , \\ &\mathbf{E}(\mathbf{X}) := \mathbf{U}(\mathbf{X}) \otimes \nabla_{\mathrm{X}} := \langle \boldsymbol{u}(\mathbf{x}) \otimes \nabla_{\mathrm{x}} \rangle_{\mathrm{V}(\mathbf{X})} \rightarrow \boldsymbol{\varepsilon}(\mathbf{X}) \equiv \tfrac{1}{2} \left(\mathbf{U}(\mathbf{X}) \otimes \nabla_{\mathrm{X}} + \mathbf{U}(\mathbf{X}) \otimes \nabla_{\mathrm{X}}{}^{\mathrm{T}} \right) \\ &\mathbf{K}(\mathbf{X}) := \boldsymbol{\varepsilon}(\mathbf{X}) \otimes \nabla_{\mathrm{X}} \rightarrow \mathrm{K_{ijk}} = \varepsilon_{\mathrm{ij,k}} = \varepsilon_{\mathrm{ji,k}} = \mathrm{K_{jik}} \end{aligned} \tag{2.2}$$

The averaging of the microscopic fields therein indicated by the bracket notaion $\langle . \rangle_{\mathrm{V}(\mathbf{X})}$ is done over a representative volume element $\mathrm{V}(\mathbf{X})$ centered around the mesoscopic point $\mathbf{X}$. The Cauchy stress and hyperstress tensors satisfy the following static equilibrium equation (inertia terms can be neglected considering the very long time scales of the bone remodeling process).

$$\left(\boldsymbol{\Sigma} - \boldsymbol{\Sigma}^{s} . \nabla_{X} \right) . \nabla_{X} + \mathbf{f} = \mathbf{0} \tag{2.3}$$

with $\mathbf{f}$ the body forces, for instance the weight.

We shall rely on the orthogonal irreducible decomposition in the present 2D context to identity the structure of the kinematic and static third-order tensors that will be involved in the growth model. The harmonic decomposition of third-order tensors (symmetrical in their first and second indices) is illustrated in Fig. 2, following [41]. The mapping T(.) represents the embedding into the space of third-order tensors (these third-order tensors will be represented in lower-dimensional tensor spaces due to their index symmetry properties). Any third-order tensor which is symmetrical in the first and second indices can be decomposed into its fully symmetric part $S_{(ijk)}$ and an asymmetrical part represented here as a second-order tensor with components R_{ij}, so that it holds

$$T_{(ij)k} = S_{(ijk)} + \frac{1}{3} \left(e_{jkl} R_{li} + e_{ikl} R_{lj} \right) \tag{2.4}$$

The tensor with components $T_{(ij)k}$ includes six independent components, namely T_{xxx}, T_{xxy}, T_{yyx}, T_{yyy}, T_{xyx}, T_{xyy}, expressed in the present 2D context and in the Cartesian basis with coordinates (x, y); the fully

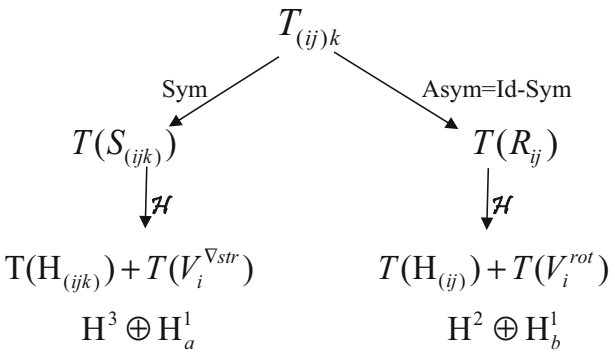

Fig. 2 Kinematic decomposition of third-order tensors into symmetric and asymmetric tensors. The mapping T(.) represents the embedding into the space of third-order tensors

symmetric third-order tensor with four independent components $\left(S_{xxx}, S_{xxy}, S_{yyx}, S_{yyy}\right)$ is next defined in equality (2.4) as

$$S_{(ijk)} = \frac{1}{3}\left(S_{(ij)k} + S_{(ki)j} + S_{(jk)i}\right) \tag{2.5}$$

The second-order tensor R_{ij} in (2.4) is the asymmetrical part of the third-order tensor $T_{(ij)k}$; it belongs to a tensor space that can further be decomposed into the space of harmonic second-order tensors denoted $\mathbb{H}^2$ and the space of vectors $\mathbb{H}_a^1$, as indicated in Fig. 2.

Note further that the duality in the sense of effective energy of $\mathbf{\Sigma^S}$ and $\mathbf{K}_e$ and in the sense of the internal virtual power of $\mathbf{\Sigma^S}$ and $\mathbf{K}$ implies that the hyperstress tensor $\mathbf{\Sigma^S}$ has the same symmetries as $\mathbf{K}$, so that it holds the index symmetry relations

$$\Sigma^{\mathrm{S}}_{\mathrm{ijk}} = \Sigma^{\mathrm{S}}_{\mathrm{jik}} \equiv \Sigma^{\mathrm{S}}_{\mathrm{(ij)k}} \tag{2.6}$$

wherein the parenthesis in the last term denotes the complete symmetry of the enclosed indices. This entails that $\mathbf{\Sigma^S}$ has six independent components given as the list

$$\mathbf{\Sigma^S} = \left(\Sigma^{\mathrm{S}}_{\mathrm{xxx}}, \Sigma^{\mathrm{S}}_{\mathrm{yyy}}, \Sigma^{\mathrm{S}}_{\mathrm{xxy}}, \Sigma^{\mathrm{S}}_{\mathrm{yxy}}, \Sigma^{\mathrm{S}}_{\mathrm{yxx}}, \Sigma^{\mathrm{S}}_{\mathrm{xyy}}\right).$$

The real vector space of completely symmetrical third-order tensors is denoted $\mathbb{S}_{(\mathrm{ijk})}$; as shown in Olive and Auffray [41], this tensor space can be decomposed into the space of harmonic third-order tensors denoted $\mathbb{H}^3$ (deviator third-order tensors) and a space of vectors $\mathbb{H}_a^1$ (the isotropic part of fully symmetrical tensors in $\mathbb{S}_{(\mathrm{ijk})}$), both of which being O(3)-irreducible spaces [41], with O(3) the orthogonal group, i.e., the group of all isometries of R3. Irreducible tensors are those tensors that cannot be further decomposed into other tensors, so that they are the elementary bricks of the complete tensor; tensors satisfying this property are called harmonic. It follows that the integrity basis for isotropic polynomial functions for $\mathbb{S}_{(\mathrm{ijk})}$ is equivalent to the integrity basis of isotropic polynomial functions of the tensor space $\mathbb{H}^3 \oplus \mathbb{H}_b^1$.

The fully symmetrical third-order tensor $\mathbb{S}_{(\mathrm{ijk})}$ decomposes into the sum

$$S_{(ijk)} = H_{(ijk)} + \frac{1}{5}\left(V_i^{\nabla str}\delta_{(jk)} + V_j^{\nabla str}\delta_{(ik)} + V_k^{\nabla str}\delta_{(ij)}\right) \tag{2.7}$$

wherein $H_{(ijk)}$ is the third-order deviator tensor represented in the space of harmonic third-order tensors $\mathbb{H}^3$ as

$$H_{(ijk)} = S_{(ijk)} - \frac{1}{5}\left(V_i^{\nabla str}\delta_{(jk)} + V_j^{\nabla str}\delta_{(ik)} + V_k^{\nabla str}\delta_{(ij)}\right) \tag{2.8}$$

The structure of this decomposition shows that the vector with two independent components $V_i^{\nabla str}$ representing the isotropic part of $\mathbb{S}_{(\mathrm{ijk})}$ writes

$$V_i^{\nabla str} = S_{(pp)i} = (T_{ppi} + 2T_{ipp}) = (3T_{111} + T_{221} + 2T_{122}, T_{112} + 2T_{211} + 3T_{222}) \tag{2.9}$$

In this formulation, the notation $V^{\nabla str}$ stands for vectors that belong to the space $\mathbb{H}^1_a$. This entails that the third-order deviator $H_{(ijk)}$ has the two independent components H_{111}, H_{222}, due to the relations

$$\begin{aligned} H_{111} = S_{111} - \frac{1}{5}V_1^{\nabla str} &= S_{111} - \frac{1}{5}\left(3T_{111} + T_{221} + 2T_{122}\right) = \left(2T_{111} - T_{221} - 2T_{122}\right)/5 \\ &= \left(2T_{111} - 3T_{122}\right)/5 = -H_{122} \\ H_{222} = S_{222} - \frac{1}{5}V_2^{\nabla str} &= S_{222} - \frac{1}{5}\left(T_{112} + 2T_{211} + 2T_{222}\right) = \left(2T_{222} - T_{112} - 2T_{211}\right)/5 \\ &= \left(2T_{222} - 3T_{112}\right)/5 = -H_{112} \end{aligned}$$

The second-order tensor with components R_{ij}, representing the asymmetric part of $T_{(ij)k}$, is decomposed as a sum of a harmonic second-order tensors in the vector space $\mathbb{H}^2$ representing the deviatoric part of R_{ij} and a vector in the space $\mathbb{H}^1_b$ representing its isotropic part, successively

$$R_{ij} = \mathrm{H}_{(ij)} + e_{ijp}V_p^{rot},\ V_i^{rot} = \frac{1}{2}\left(T_{ppi} - T_{ipp}\right) \tag{2.10}$$

with e_{ijp} the Levi–Civita permutation tensor and $H_{(ij)}$ a second-order deviator represented in the space of harmonic second order tensors $\mathbb{H}^2$ in the following form

$$\mathrm{H}_{(ij)} = R_{ij} - e_{ijp}V_p^{rot} \tag{2.11}$$

Thus, summarizing previous developments, any third-order symmetrical tensor in 2D space, with components $T_{(ij)k}$, is fully characterized by six independent quantities represented in the direct sum of harmonic spaces $\mathbb{H}^3 \oplus \mathbb{H}^1_a$, $\mathbb{H}^2 \oplus \mathbb{H}^1_b$ embedded into third-order tensors with the operator $T(.)$. Note that in the present 2D context, the antisymmetrical tensor $e_{ijp}V_p^{rot}$ vanishes.

In order to be more specific, we express the geometrical picture of third-order tensors symmetrical in their first and second indices using the following representation:

$$\hat{\underset{\sim}{\mathrm{T}}} = \hat{\mathrm{T}}_{\alpha k}\hat{\mathrm{e}}_\alpha \otimes \mathrm{e}_k,\ 1 \le \alpha \le 3,\ 1 \le k \le 2 \tag{2.12}$$

with the introduced basis of symmetrical tensors therein

$$\hat{\mathrm{e}}_\alpha = \left(\frac{1-\delta_{ij}}{\sqrt{2}} + \frac{\delta_{ij}}{2}\right)\left(\mathrm{e}_i \otimes \mathrm{e}_j + \mathrm{e}_j \otimes \mathrm{e}_i\right)\ 1 \le \alpha \le 3 \tag{2.13}$$

Using orthonormal basis (2.13), the relationship between the matrix components $\hat{\mathrm{T}}_{\alpha k}$ and T_{ijk} is specified by

$$\hat{\mathrm{T}}_{\alpha k} = \begin{cases} \mathrm{T}_{ijk} & \text{if } i = j \\ \sqrt{2}\mathrm{T}_{ijk} & \text{if } i \neq j \end{cases} \tag{2.14}$$

Therefore, we obtain the following matrix representation:

$$\mathrm{T}_{(\mathrm{ij})\mathrm{k}} = \begin{pmatrix} \mathrm{T}_{111} & \mathrm{T}_{112} \\ \mathrm{T}_{221} & \mathrm{T}_{222} \\ \sqrt{2}\mathrm{T}_{121} & \sqrt{2}\mathrm{T}_{122} \end{pmatrix} \tag{2.15}$$

The decomposition into a symmetrical and an asymmetrical tensor writes:

$$\mathrm{T}\left(\mathrm{S}_{(\mathrm{ijk})}\right) = \begin{pmatrix} \mathrm{T}_{111} & \frac{1}{3}(\mathrm{T}_{112} + 2\mathrm{T}_{121}) \\ \frac{1}{3}(\mathrm{T}_{221} + 2\mathrm{T}_{122}) & \mathrm{T}_{222} \\ \frac{\sqrt{2}}{3}(\mathrm{T}_{112} + 2\mathrm{T}_{121}) & \frac{\sqrt{2}}{3}(\mathrm{T}_{221} + 2\mathrm{T}_{122}) \end{pmatrix},\quad \mathrm{T}\left(\mathrm{R}_{(\mathrm{ij})}\right) = \begin{pmatrix} 0 & \frac{2}{3}(\mathrm{T}_{112} - \mathrm{T}_{121}) \\ \frac{2}{3}(\mathrm{T}_{221} - \mathrm{T}_{122}) & 0 \\ \frac{\sqrt{2}}{3}(\mathrm{T}_{121} - \mathrm{T}_{112}) & \frac{\sqrt{2}}{3}(\mathrm{T}_{122} - \mathrm{T}_{221}) \end{pmatrix} \tag{2.16}$$

Symmetrical part (4 independent components) Asymmetrical part (2 independent components)

The harmonic decomposition of the fully symmetrical tensor $S_{(ijk)}$ writes:

$$\mathrm{T}\left(\mathrm{S}_{(ijk)}\right) = \begin{cases} \mathrm{T}\left(\mathrm{H}_{(ijk)}\right) = \begin{pmatrix} \frac{1}{4}\left(2\mathrm{T}_{111} - 3\mathrm{T}_{122}\right) & -\frac{1}{6}\left(2\mathrm{T}_{222} - 3\mathrm{T}_{112}\right) \\ -\frac{1}{6}\left(2\mathrm{T}_{111} - 3\mathrm{T}_{122}\right) & \frac{1}{4}\left(2\mathrm{T}_{222} - 3\mathrm{T}_{112}\right) \\ -\frac{\sqrt{2}}{12}\left(2\mathrm{T}_{222} - 3\mathrm{T}_{112}\right) & -\frac{\sqrt{2}}{12}\left(2\mathrm{T}_{111} - 3\mathrm{T}_{122}\right) \end{pmatrix} \\ + \\ \mathrm{T}\left(\mathrm{V}_{i}^{\nabla \mathrm{str}}\right) = \begin{pmatrix} \frac{1}{4}\left(2\mathrm{T}_{111} + 3\mathrm{T}_{122}\right) & \frac{1}{6}\left(2\mathrm{T}_{222} + 3\mathrm{T}_{112}\right) \\ \frac{3}{15}\left(2\mathrm{T}_{111} + 3\mathrm{T}_{122}\right) & \frac{1}{4}\left(2\mathrm{T}_{222} + 3\mathrm{T}_{112}\right) \\ \frac{\sqrt{2}}{12}\left(2\mathrm{T}_{222} + 3\mathrm{T}_{112}\right) & \frac{\sqrt{2}}{12}\left(2\mathrm{T}_{111} + 3\mathrm{T}_{122}\right) \end{pmatrix} \end{cases} \tag{2.17}$$

The decomposition of the asymmetrical part of $T_{(ij)k}$ writes:

$$\mathrm{T}\left(\mathrm{R}_{ij}\right) = \begin{cases} \mathrm{T}\left(\mathrm{H}_{(ij)}\right) = \begin{pmatrix} 0 & \frac{1}{3}\left(\mathrm{T}_{112} - \mathrm{T}_{121}\right) \\ \frac{1}{3}\left(\mathrm{T}_{221} - \mathrm{T}_{122}\right) & 0 \\ \frac{\sqrt{2}}{6}\left(\mathrm{T}_{121} - \mathrm{T}_{112}\right) & \frac{\sqrt{2}}{6}\left(\mathrm{T}_{122} - \mathrm{T}_{221}\right) \end{pmatrix} + \\ \mathrm{T}\left(\mathrm{V}_{i}^{\mathrm{rot}}\right) = \begin{pmatrix} 0 & \frac{1}{3}\left(\mathrm{T}_{112} - \mathrm{T}_{121}\right) \\ \frac{1}{3}\left(\mathrm{T}_{221} - \mathrm{T}_{122}\right) & 0 \\ \frac{\sqrt{2}}{6}\left(\mathrm{T}_{121} - \mathrm{T}_{112}\right) & \frac{\sqrt{2}}{6}\left(\mathrm{T}_{122} - \mathrm{T}_{221}\right) \end{pmatrix} \end{cases} \tag{2.18}$$

As a summary, the isotropic part of the tensor $\mathrm{T}_{(ij)k}$ has the following two independent components:

$$\left(2\mathrm{T}_{111} + 3\mathrm{T}_{122}\right), \left(2\mathrm{T}_{222} + 3\mathrm{T}_{112}\right)$$

The deviatoric part of the tensor $\mathbf{T}_{(ij)k}$ is characterized by the following four independent components:

$$\mathrm{T}_{111}, \mathrm{T}_{222}, \left(\mathrm{T}_{112} - \mathrm{T}_{121}\right), \left(\mathrm{T}_{221} - \mathrm{T}_{122}\right).$$

The second gradient elastic and growth rate of deformation tensors has the same structure as the total second gradient rate of deformation tensor, so that they are each characterized by two independent components for their isotropic part and four independent components for their deviatoric part.

2.2 Growth kinematics

We first define an average growth velocity gradient at the first order based on boundary values of the surface growth velocity field $\mathbf{V}_g$ as

$$\overline{\mathbf{L}}_g := \frac{1}{|\mathrm{V}|} \int_{\partial \mathrm{V}_B} \mathbf{V}_g \otimes \mathbf{N} \mathrm{dS} \tag{2.19}$$

with |V| the volume measure of the two-phase domain including trabecular bone and matrix phase. Relation (2.19) follows from the fact that the velocity of the interface, vector $\mathbf{V}_g$, has a support restricted to the domain of the bone tissue boundary ∂V_B.

The previous form of $\overline{\mathbf{L}}_g$ leads to the elaboration of the average first gradient rate of growth tensor over the whole domain as

$$\overline{\mathbf{D}}_{1g} := \frac{1}{2}\left(\overline{\mathbf{L}}_g + \overline{\mathbf{L}}_g^T\right) = \frac{1}{|V|}\int\limits_{\partial V_B} \frac{1}{2}\left(\mathbf{V}_g \otimes \mathbf{N} + \mathbf{N} \otimes \mathbf{V}_g\right) dS \equiv \overline{\mathbf{D}}_{1gB} \tag{2.20}$$

Moreover, application of the divergence theorem to the velocity field in the entire domain gives

$$\int\limits_V \text{grad}\mathbf{V} dX = \int\limits_{\partial V} \mathbf{V} \otimes \mathbf{N} dS \tag{2.21}$$

wherein the velocity field $\mathbf{V}$ on the inclusion boundary represents the velocity of material points there and should not be confused with the geometrical interface velocity due to growth, vector $\mathbf{V}_g$. The difference $\mathbf{V} - \mathbf{V}_g$ with support the interface domain ∂V_B represents the relative velocity of material points crossing the interface. The volumetric growth rate is elaborated from the time variation of the volume of grown material, the scalar

$$\Gamma(\mathbf{x}, t) := \frac{1}{|\Omega_g|}\frac{D}{Dt}|\Omega_g| = \frac{1}{|\Omega_g|}\int\limits_{\partial B_\varepsilon} \mathbf{V}_g.\mathbf{N} dS \tag{2.22}$$

Similarly, the first gradient average rate of deformation tensor is elaborated as

$$\overline{\mathbf{D}}_1 := \frac{1}{|V|}\int\limits_V \mathbf{D}_1 dX = \frac{1}{|V|}\int\limits_{\partial V} \frac{1}{2}\left(\mathbf{V} \otimes \mathbf{N} + \mathbf{N} \otimes \mathbf{V}\right) dS \tag{2.23}$$

The first gradient average elastic rate of deformation tensor is then defined as the difference between the average total rate of deformation tensor and its growth part at the first order

$$\overline{\mathbf{D}}_{1e} := \overline{\mathbf{D}}_1 - \overline{\mathbf{D}}_{1g} \tag{2.24}$$

which would coincide with $\overline{\mathbf{D}}$ in the absence of growth, and it characterizes the stored reversible strains within the RVE. It is thus associated with residual stresses, namely stresses, that remain within the domain after unloading.

The volume fractions of bone tissue and surrounding matrix, respectively, elaborated as

$$f_B := \frac{V_B}{V}, f_M := \frac{V_M}{V} \rightarrow f_B + f_M = 1 \tag{2.25}$$

We can further split the overall (averaged) total gradient velocity tensor into separate contributions from the bone and matrix, as

$$\overline{\mathbf{D}}_1 := \frac{1}{V}\int\limits_V \mathbf{D}_1 dX = \frac{1}{V}\int\limits_{V_B} \mathbf{D}_1 dX + \frac{1}{V}\int\limits_{V_M} \mathbf{D}_1 dX \equiv f_B\overline{\mathbf{D}}_{1B} + f_M\overline{\mathbf{D}}_{1M} \tag{2.26}$$

with the bone tissue and matrix, total rates of deformation tensors are defined as

$$\overline{\mathbf{D}}_B := \frac{1}{|V_B|}\int\limits_{V_B} \mathbf{D} dX,\ \overline{\mathbf{D}}_M := \frac{1}{|V_M|}\int\limits_{V_M} \mathbf{D} dX \tag{2.27}$$

A similar decomposition is supposed to hold for the average elastic rate of deformation tensor

$$\overline{\mathbf{D}}_{1e} := f_B\overline{\mathbf{D}}_{1eB} + f_M\overline{\mathbf{D}}_{1eM} \tag{2.28}$$

From (2.27) and (2.28), the decomposition of the average total velocity gradient into the average growth and elastic contributions into both growing phase and matrix

$$\overline{\mathbf{D}}_1 = \overline{\mathbf{D}}_{1g} + \left(f_B \overline{\mathbf{D}}_{1eB} + f_M \overline{\mathbf{D}}_{1eM}\right) \tag{2.29}$$

Now, we turn to the second-order average kinematics. By analogy, the average second gradient rate of growth can be constructed as the following third-order tensor

$$\overline{\dot{\mathbf{K}}}_g := \frac{1}{|V|}\int_{\partial V_B} \left(\mathbf{V}_g \otimes \nabla_x\right) \otimes \mathbf{N} dS \equiv \frac{1}{|V|}\int_{V_B} \left(\mathbf{V}_g \otimes \nabla_x\right) \otimes \nabla_x dV \rightarrow \left(\dot{K}_g\right)_{ijk} = \left(\dot{K}_g\right)_{ikj} \tag{2.30}$$

Note that there is no way to fully express $\overline{\dot{\mathbf{K}}}_g$ versus the growth velocity only, since its microscopic gradient also intervenes; the transformation of the surface to volume integral in (2.30) is possible since we assume that surface remodeling is a fully irreversible process so that the surface remodeling field is compatible.
The integrand in the surface integral of the first equality of (2.30) is further elaborated as

$$\mathbf{V}_g \otimes \nabla_x \equiv \mathbf{V}_g \otimes \nabla_S + \nabla_N V \otimes \mathbf{N} \leftrightarrow \partial_j V_{gi} = \left(\nabla_{Sj} + N_j \nabla_N\right) V_{gi} \tag{2.31}$$

denoting therein

$$\nabla_N := N_j \frac{\partial}{\partial x_j}, \nabla_S := \nabla_x - N_j \nabla_N \tag{2.32}$$

successively the normal gradient and tangential derivative. Relying next on the following decomposition of the velocity field into tangential and normal contributions, viz.

$$V_N := \mathbf{V}_g.\mathbf{N} \rightarrow \mathbf{V}_{gT} = \mathbf{V}_g - V_N \mathbf{N} \tag{2.33}$$

a straightforward calculation relying on the decomposition (2.33) then leads to the following simplified form of the growth velocity gradient in (2.31):

$$\mathbf{V}_g \otimes \nabla_x \equiv \mathbf{V}_g \otimes \nabla_S + \nabla_N V \otimes \mathbf{N} \leftrightarrow \partial_j V_{gi} = \nabla_{Sj} V_{gTi} + N_i N_j \nabla_N V_N - V_N L_{ij} \tag{2.34}$$

involving the curvature tensor (otherwise called Weingarten map) $\mathbf{L} \in \mathrm{Lin}\left(\mathbf{n}, \mathbf{n}^{\perp}\right)$ viewed as a linear mapping onto the tangent plane

$$L_{ij} := -\nabla_S \mathbf{N} \tag{2.35}$$

The symmetrized form of $\overline{\mathbf{K}}_g$ (obtained by symmeterization of the two first indices) leads to the elaboration of the average second gradient rate of growth tensor over the whole domain as

$$\overline{\mathbf{D}}_{2g} := \frac{1}{2}\left(\overline{\mathbf{K}}_g + \overline{\mathbf{K}}_g^T\right) \tag{2.36}$$

in which the transpose is done on the first and second indices. Due to (2.2) and (2.30), tensor $\overline{\mathbf{D}}_{2g}$ has the following symmetries:

$$\left(\overline{D}_{2g}\right)_{ijk} = \left(\overline{D}_{2g}\right)_{jik} = \left(\overline{D}_{2g}\right)_{ikj} \tag{2.37}$$

Similar decompositions written for the composite domain made of the trabeculae and the surrounding matrix hold for the second gradient average total rate of deformation tensor, viz.

$$\overline{\mathbf{D}}_2 = \overline{\mathbf{D}}_{2g} + \left(f_B \overline{\mathbf{D}}_{2eB} + f_M \overline{\mathbf{D}}_{2eM}\right) \tag{2.38}$$

The second gradient elastic rate of deformation then is evaluated as the difference

$$\overline{\mathbf{D}}_{2e} := \overline{\mathbf{D}}_2 - \overline{\mathbf{D}}_{2g} \tag{2.39}$$

Tensor $\overline{\mathbf{D}}_{2e}$ inherits the symmetries of tensors $\overline{\mathbf{D}}_2$, $\overline{\mathbf{D}}_{2g}$, so that it holds the following equalities

$$\left(\overline{D}_{2e}\right)_{ijk} = \left(\overline{D}_{2e}\right)_{jik} = \left(\overline{D}_{2e}\right)_{ikj} \tag{2.40}$$

3 Model for external remodeling based on Eshelby stress

At the microscale of the trabecular bone struts, one shall formulate a surface growth model in the framework of Cauchy bulk and surface elasticity, in order to link the surface remodeling velocity to the identified conjugated driving force. We recall the main ingredients of the microscale trabecular surface remodeling model elaborated in Louna et al. [34], sustained by the surface growth models developed in [17,18,25].

From a kinematic point of view, and adopting unless otherwise stated a large strains formalism, the surface deformation gradient is divided multiplicatively into a surface growth mapping $\tilde{\mathbf{F}}_{\mathrm{g}}$ and an accommodation mapping $\tilde{\mathbf{F}}_{\mathrm{a}}$ needed to restore the kinematic compatibility; hence, it holds the multiplicative decomposition

$$\tilde{\mathbf{F}} = \tilde{\mathbf{F}}_{\mathrm{a}}.\tilde{\mathbf{F}}_{\mathrm{g}} \tag{3.1}$$

The surface mapping $\tilde{\mathbf{F}} := \mathbf{F}.\boldsymbol{\Pi}$ represents the projection of the bulk transformation gradient onto the tangent plane of $\partial\Omega$, with $\boldsymbol{\Pi} = \mathbf{I}_{\mathrm{S}} - \mathbf{N}\otimes\mathbf{N}$ the corresponding projector, with the second-order tensor $\mathbf{I}_{\mathrm{S}}$ denoting the surface identity tensor, mapping any vector in the tangent plane to the surface to itself. A generic point on the boundary is denoted. Previous multiplicative decomposition induces a decomposition of the Jacobean of the total transformation, viz.

$$\tilde{\mathrm{J}} = \tilde{\mathrm{J}}_{\mathrm{a}}\tilde{\mathrm{J}}_{\mathrm{g}} \tag{3.2}$$

with $\tilde{\mathrm{J}}_{\mathrm{a}} := \det\left(\tilde{\mathbf{F}}_{\mathrm{a}}\right)$; $\tilde{\mathrm{J}}_{\mathrm{g}} := \det\left(\tilde{\mathbf{F}}_{\mathrm{g}}\right)$, respectively, the growth and accommodation Jacobean, such that the surface densities in the reference and actual configurations, quantities $\rho_{0\mathrm{S}}$, ρ_{S}, respectively, are related by

$$\rho_{0\mathrm{S}} = \tilde{\mathrm{J}}_{\mathrm{a}}\rho_{\mathrm{S}} \tag{3.3}$$

One assumes following [34] that mass is preserved between the intermediate and actual configurations (growth of mass only occurs between the initial and intermediate configuration).

Mechanical equilibrium of the growing surface writes as the following balance of surface momentum

$$\begin{cases} \nabla_{\mathrm{S}}.\tilde{\boldsymbol{\Sigma}}_{\mathbf{a}} - \boldsymbol{\Pi}.\mathbf{K}^{\mathrm{T}}.\frac{\partial \mathrm{W}^{\mathrm{S}}}{\partial \mathrm{N}} + \tilde{\mathbf{F}}^{\mathrm{T}}.\mathbf{f}_{\mathrm{S}} = \mathbf{0} \text{ on } \Omega_{\mathrm{g}} \\ \mathbf{f}_{\mathrm{S}} = \mathbf{0} \text{ on } \Omega_{\mathrm{g}}\backslash\Omega_{\mathrm{t}} \end{cases} \tag{3.4}$$

with $\mathbf{R} := -\nabla_R\mathbf{N}$ the curvature tensor of the surface, $\nabla_{\mathrm{S}} = \boldsymbol{\Pi}.\nabla$ the surface gradient, and the surface Eshelby stress therein defined as

$$\tilde{\boldsymbol{\Sigma}}_{\mathrm{a}} := \mathrm{W}^{\mathrm{s}}\mathbf{I}_{\mathrm{s}} - \tilde{\mathbf{F}}_{\mathrm{a}}^{\mathrm{T}}.\tilde{\mathbf{T}} \tag{3.5}$$

with $\tilde{\mathbf{F}}_{\mathrm{a}}$ and $\tilde{\mathbf{T}} := \frac{\partial \mathrm{W}^{\mathrm{s}}}{\partial \tilde{\mathbf{F}}_{\mathrm{a}}}$ the elastic surface mapping needed to restore the surface compatibility and the surface stress, respectively. The surface position and its variation on S_{g} are denoted $\mathbf{X}_{\mathrm{S}}$ and $\delta\mathbf{X}_{\mathrm{S}}$, respectively.

The surface mass balance equation expresses as

$$\begin{aligned} &\dot{\rho}_{\mathrm{g}} = \Gamma^{\mathrm{S}}\rho_{\mathrm{g}} \text{ on } \Omega_{\mathrm{g}} \\ &\Gamma^{\mathrm{S}} = \mathrm{Tr}\left(\nabla\tilde{\mathbf{V}}_{\mathrm{g}}\right) = \mathrm{tr}\left(\dot{\tilde{\mathbf{F}}}_{\mathrm{g}}.\tilde{\mathbf{F}}_{\mathrm{g}}^{-1}\right) = \frac{\tilde{\mathrm{B}}}{\rho_{\mathrm{g}}^{2}}\mathrm{tr}\left(\boldsymbol{\Sigma}_{\mathrm{a}}(\boldsymbol{\varepsilon}_{\mathrm{a}}) - \boldsymbol{\Sigma}_{0}\right) \\ &\rho_{\mathrm{g}}\left(\mathbf{X}, \mathrm{t}=0\right) = \rho_{0}\left(\mathbf{X}\right) \end{aligned} \tag{3.6}$$

with ρ_{S} the surface density, Γ^{S} the rate of mass growth, given by the trace of the surface growth velocity gradient, and $\tilde{\mathbf{V}}_{\mathrm{g}}$ the surface growth velocity.

Following developments detailed in Louna et al. [34], the following residual surface dissipation is obtained, considering the case of a purely mechanical dissipation so that spatial derivation of the surface growth velocity field makes sense:

$$\int_{\mathrm{S}_{\mathrm{g}}} \nabla_{\mathrm{S}}.\left(\tilde{\boldsymbol{\Sigma}}_{\mathrm{a}}\right).\tilde{\mathbf{V}}_{\mathrm{g}}\mathrm{dS} \geq 0 \tag{3.7}$$

The following linear surface growth model is next formulated as a sufficient condition for the dissipation to be nonnegative,

$$\tilde{\mathbf{V}}_{\mathrm{g}} = \tilde{\mathrm{K}}\mathrm{div}_{\mathrm{S}}\left(\tilde{\boldsymbol{\Sigma}}_{\mathrm{a}}\right),\ \tilde{\mathrm{K}} \geq 0 \tag{3.8}$$

with $\tilde{\mathrm{K}}$ a nonnegative constant determining the surface growth kinetics. The residual dissipation represents the surface dissipation due to surface growth, deemed as an irreversible contribution.

The bone adaptation algorithm relies on the solution of a linear elasticity problem in the bulk one, coupled to the surface growth problem, elaborated in [25]. The bulk equilibrium elasticity problem writes as follows:

$$\begin{cases} \mathrm{div}\boldsymbol{\sigma} + \rho\mathbf{g} = \mathbf{0} \text{ in } \Omega \\ \boldsymbol{\Sigma}_{\mathrm{a}} = \mathrm{W}_0\mathbf{I} - \boldsymbol{\varepsilon}_{\mathrm{a}}^{\mathrm{T}}.\boldsymbol{\sigma} \\ \mathbf{U} = \mathbf{0} \text{ on } \Omega_{\mathrm{u}};\ \boldsymbol{\sigma}.\mathbf{N} = \mathbf{f}_{\mathrm{S}} \text{ on } \Omega_{\mathrm{t}} \\ \boldsymbol{\sigma} = 2\mu\left(\rho\right)\boldsymbol{\varepsilon}_{\mathrm{a}} + \lambda\left(\rho\right)\mathrm{Tr}\left(\boldsymbol{\varepsilon}_{\mathrm{a}}\right)\mathbf{I} \end{cases} \tag{3.9}$$

The surface constitutive law is prescribed from a surface elastic density per unit volume, assuming an isotropic growing surface with two material parameters:

$$\begin{cases} \mathrm{W}^{\mathrm{S}} = \frac{\lambda(\rho)}{2}\mathrm{Tr}(\tilde{\boldsymbol{\varepsilon}}_{\mathrm{a}})^2 + \mu\left(\rho\right)\left(\tilde{\boldsymbol{\varepsilon}}_{\mathrm{a}} : \tilde{\boldsymbol{\varepsilon}}_{\mathrm{a}}\right) \\ \tilde{\boldsymbol{\Sigma}}_{\mathbf{a}} = \mathrm{W}^{\mathrm{S}}\boldsymbol{\Pi} - \tilde{\boldsymbol{\varepsilon}}_{\mathrm{a}}^{\mathrm{T}}.\frac{\partial \mathrm{W}^{\mathrm{S}}}{\partial \tilde{\boldsymbol{\varepsilon}}_{\mathrm{a}}} \end{cases} \tag{3.10}$$

The two bulk and surface problems are solved in a staggered manner; the solution of bulk problem provides at each time step the stress field on each point in the domain including the surface, leading in turn to an evaluation of the remodeling velocity given versus the divergence of Eshelby stress.

In this work, we consider a constant reference value for bone formation of the order of $\varepsilon_0 = 2 \times 10^{-3}$ [39]: This value represents the minimum strain for remodeling to occur. The trabeculae are in fact composed of packets of remodeled bone of different ages and therefore different degrees of mineralization; this may lead to a non-uniform mineral distribution within the trabecular strut, which in turn leads to a variation of trabecular tissue stiffness. Based on this, the homogenized Young's modulus (GPa) of the trabecular bone tissue versus the tissue density (g/cm^3) is determined as [24,48]

$$\mathrm{E}\left(\rho\right) = 6.5\rho^2 + 12.3\rho - 26.5 \tag{3.11}$$

This expression is used within the tissue density range $1.3 \leq \rho \leq 2$. The Poisson's ratio of trabecular tissue material is taken to be 0.3. Furthermore, we adopt in all simulations $\mathrm{E}\left(\rho\right)\varepsilon_0$ as the stress level that promotes the remodeling.

The evaluation of the average kinematics over the RVE a representative unit cell of trabecular bone relies on previously written equations. The next sections will be devoted to the setting up of a constitutive growth model extended up to second gradient effects and to numerical results showing the influence of both the first- and second-order applied stress on the development of bone growth.

4 Determination of an effective second gradient growth model based on a micromechanical analysis

4.1 Structure of the kinematic tensors in small strains

Since we restrict to a small strain and strain rate framework in the present context of bone remodeling, the average kinematic first and second gradient tensors $\mathbf{E}\left(\mathbf{X}\right)$ and $\mathbf{K}\left(\mathbf{X}\right)$ introduced in (2.2) can be assimilated to their small strain versions, and thus, one is entitled to use the symmetrized tensors

$$\begin{array}{l} \boldsymbol{\varepsilon}\left(\mathbf{X}\right) \equiv \frac{1}{2}\left(\mathbf{U}\left(\mathbf{X}\right) \otimes \nabla_{\mathrm{X}} + \mathbf{U}\left(\mathbf{X}\right) \otimes \nabla_{\mathrm{X}}{}^{\mathrm{T}}\right) \rightarrow \varepsilon_{\mathrm{ij}} = \varepsilon_{\mathrm{ji}} \\ \mathbf{k}\left(\mathbf{X}\right) := \boldsymbol{\varepsilon}\left(\mathbf{X}\right) \otimes \nabla_{\mathrm{X}} \rightarrow \mathrm{k}_{\mathrm{ijk}} = \varepsilon_{\mathrm{ij,k}} = \varepsilon_{\mathrm{ji,k}} = \mathrm{k}_{\mathrm{jik}} \end{array} \tag{4.1}$$

Note especially that we use in (4.1) the symmetrized form (with respect to the first and second indices) of the second gradient of the displacement field $\mathbf{k}$.

The center of gravity of the mesoscopic volume element $\mathrm{V}\left(\mathbf{X}\right)$ over which averaging is done is denoted by the upper case symbol $\mathbf{X}$; it has to be distinguished from the microscopic spatial variable $\mathbf{x}$ over which averaging is done within $\mathrm{V}\left(\mathbf{X}\right)$.

In the sequel, we shall use the following notations for the first and second gradient total, elastic and growth mappings in line with (4.1):

$$\mathbf{E} := \overline{\boldsymbol{\varepsilon}}_1,\ \mathbf{k} := \overline{\boldsymbol{\varepsilon}}_2,\ \mathbf{E}_e := \overline{\boldsymbol{\varepsilon}}_{1e},\ \mathbf{k}_e := \overline{\boldsymbol{\varepsilon}}_{2e},\ \mathbf{E}_g := \overline{\boldsymbol{\varepsilon}}_{1g},\ \mathbf{k}_g := \overline{\boldsymbol{\varepsilon}}_{2g} \tag{4.2}$$

Since bone growth at the mesoscopic level is a slow process occurring at a typical timescale of a few weeks, one can further linearize the average strain rates introduced in (2.2) and in (2.30) through (2.33) and approximate them by their small strains rates counterparts; it accordingly holds the following approximations (the index 2 in any tensor therein indicates a third-order tensor representative of second gradient effects)

$$\begin{aligned}
&\overline{\mathbf{D}}_1 \cong \overline{\dot{\boldsymbol{\varepsilon}}}_1 = \dot{\mathbf{E}},\ \overline{\mathbf{D}}_{1g} \cong \overline{\dot{\boldsymbol{\varepsilon}}}_{1g} = \dot{\mathbf{E}}_g,\ \overline{\mathbf{D}}_{1e} \cong \overline{\dot{\boldsymbol{\varepsilon}}}_{1e} = \dot{\mathbf{E}}_e \rightarrow \overline{\mathbf{D}}_1 = \overline{\mathbf{D}}_{1g} + \overline{\mathbf{D}}_{1e} \\
&\overline{\mathbf{D}}_2 \cong \overline{\dot{\boldsymbol{\varepsilon}}} \otimes \nabla = \overline{\dot{\boldsymbol{\varepsilon}}}_2,\ \overline{\mathbf{D}}_{2g} \cong \overline{\dot{\boldsymbol{\varepsilon}}}_g \otimes \nabla = \overline{\dot{\boldsymbol{\varepsilon}}}_{2g},\ \overline{\mathbf{D}}_{2e} \cong \overline{\dot{\boldsymbol{\varepsilon}}}_e \otimes \nabla = \overline{\dot{\boldsymbol{\varepsilon}}}_{2e} \rightarrow \overline{\mathbf{D}}_2 = \overline{\mathbf{D}}_{2g} + \overline{\mathbf{D}}_{2e}
\end{aligned} \tag{4.3}$$

Considering (4.3), this entails the following additive split of the total strain rate tensor and a similar one written for the second gradient counterpart

$$\begin{aligned}
\dot{\mathbf{E}} &= \dot{\mathbf{E}}_g + \dot{\mathbf{E}}_e \\
\dot{\mathbf{k}} &= \dot{\mathbf{k}}_e + \dot{\mathbf{k}}_g
\end{aligned} \tag{4.4}$$

The first- and second-order stress tensors at the mesoscopic level of the unit cell are elaborated as averaging of their microscopic counterpart defined in Sect. 2.
Due furthermore to small strain rates, time derivatives and spatial averaging commute, so the introduced averaged second gradient elastic rate of deformation and second gradient growth rate of deformation tensors write as

$$\begin{aligned}
&\overline{\mathbf{D}}_1 = \dot{\mathbf{E}},\ \overline{\mathbf{D}}_{1g} = \dot{\mathbf{E}}_g,\ \overline{\mathbf{D}}_{1e} = \dot{\mathbf{E}}_e, \\
&\overline{\mathbf{D}}_2 = \dot{\mathbf{k}},\ \overline{\mathbf{D}}_{2g} = \dot{\mathbf{k}}_g,\ \overline{\mathbf{D}}_{2e} = \dot{\mathbf{k}}_e
\end{aligned} \tag{4.5}$$

Remark: The average second gradient rate of elastic deformation tensor is not the spatial gradient of the first gradient rate of elastic deformation tensor. This third-order tensor is rather evaluated as a difference of the total second gradient rate of deformation tensor and the average second gradient rate of growth deformation tensor.

4.2 Second gradient growth model in the framework of irreversible thermodynamics

Since one expects a priori both an effect of first and second gradient kinematic controls applied over the unit cell, one is entitled to write general constitutive models for bone growth in multiplicative form decoupling the effect of effective bone density and external stress as follows

$$\begin{pmatrix} \overline{\mathbf{D}}_{1g} \\ \overline{\mathbf{D}}_{2g} \end{pmatrix} = g\left(\rho^{\text{eff}}\right) \begin{pmatrix} \mathbf{h}_1\left(\boldsymbol{\Sigma}^{\text{ext}}, \boldsymbol{\Sigma}^{\mathbf{S},\text{ext}}\right) \\ \mathbf{h}_2\left(\boldsymbol{\Sigma}^{\text{ext}}, \boldsymbol{\Sigma}^{\mathbf{S},\text{ext}}\right) \end{pmatrix} \tag{4.6}$$

with $g\left(\rho^{\text{eff}}\right)$ and $\mathbf{h}_1\left(\boldsymbol{\Sigma}^{\text{ext}}, \boldsymbol{\Sigma}^{\mathbf{S},\text{ext}}\right), \mathbf{h}_2\left(\boldsymbol{\Sigma}^{\text{ext}}, \boldsymbol{\Sigma}^{\mathbf{S},\text{ext}}\right)$, respectively, scalar-valued and tensor-valued functions of their respective arguments, the form of which shall be specific later on. Note that although the unit cell is subjected to a kinematic control over its boundary, the effective growth constitutive model is written based on the stress and hyperstress tensors (computed as reaction 'forces') as mechanical triggers of growth. The obtained average elastic constitutive law evaluates the stress and hyperstress tensors for each microstructural state (the microstructure is frozen, so that one solves in fact an elastic problem with a kinematic control including strain and strain gradient).

A proper form of the second gradient growth model is obtained from the expression of the local dissipation reflected by Clausius–Duhem inequality, adopting the framework of generalized standard materials. The effective material is characterized by a free energy density sum of elastic and growth contributions, each of them depending on the average first and second gradient of the elastic and growth average deformation tensors

$$\psi = \psi_e\left(\mathbf{E}_e, \mathbf{K}_e\right) + \psi_g\left(\mathbf{E}_g, \mathbf{K}_g\right) \tag{4.7}$$

Note that the growth deformations are here considered as internal variables associated with a purely dissipative behavior. The elastic potential of deformation involves the effective first and second gradient moduli, successively the fourth- and sixth-order tensors $\mathbf{C}$, $\mathbf{D}$, so that it writes for a centrosymmetric microstructure

$$\psi_e\left(\mathbf{E}_e, \mathbf{K}_e\right) = \frac{1}{2}\mathbf{E}_e : \mathbf{C} : \mathbf{E}_e + \frac{1}{2}\mathbf{K}_e \dot{:} \mathbf{D} \dot{:} \mathbf{K}_e \tag{4.8}$$

The virtual power of internal forces writes after elementary calculations due to the introduced additive split of the average strain rates as

$$\mathrm{P_i} = -\boldsymbol{\Sigma} : \dot{\overline{\boldsymbol{\varepsilon}}}_{1e} - \boldsymbol{\Sigma} : \dot{\overline{\boldsymbol{\varepsilon}}}_{1g} - \boldsymbol{\Sigma}^{\mathbf{S}} \dot{:} \dot{\overline{\boldsymbol{\varepsilon}}}_{2e} - \boldsymbol{\Sigma}^{\mathbf{S}} \dot{:} \dot{\overline{\boldsymbol{\varepsilon}}}_{2g} \tag{4.9}$$

Recalling the additive split of the strain rate tensor written in (4.3), the virtual power of internal forces writes after elementary calculations due to the introduced additive split of the average strain rates as

$$\mathrm{P_i} = -\boldsymbol{\Sigma} : \overline{\mathbf{D}}_{1e} - \boldsymbol{\Sigma} : \overline{\mathbf{D}}_{1g} - \boldsymbol{\Sigma}^{\mathbf{S}} \dot{:} \overline{\mathbf{D}}_{2e} - \boldsymbol{\Sigma}^{\mathbf{S}} \dot{:} \overline{\mathbf{D}}_{2g} \tag{4.10}$$

with $\boldsymbol{\Sigma}$, $\boldsymbol{\Sigma}^{\mathbf{S}}$ the Cauchy stress and hyperstress tensors, respectively, a second-order and a third-order tensor. The local dissipation writes after identification of the first- and second-order constitutive laws as

$$\Phi = -\mathrm{P_i} - \dot{\psi} = \left(\boldsymbol{\Sigma} : \overline{\mathbf{D}}_{1e} + \boldsymbol{\Sigma}^{\mathbf{S}} \dot{:} \overline{\mathbf{D}}_{2e} - \dot{\psi}_e\right) + \boldsymbol{\Sigma} : \overline{\mathbf{D}}_{1g} + \boldsymbol{\Sigma}^{\mathbf{S}} \dot{:} \overline{\mathbf{D}}_{2g} - \dot{\psi}_g \geq 0 \tag{4.11}$$

Following the standard Coleman–Noll procedure, the first part of the local dissipation in (4.11) delivers the constitutive law, due to the introduced elastic potential in (4.8):

$$\boldsymbol{\Sigma} := \frac{\partial \psi_e\left(\mathbf{E}_e, \mathbf{K}_e\right)}{\mathbf{E}_e} = \mathbf{C} : \mathbf{E}_e, \ \boldsymbol{\Sigma}^{\mathbf{S}} := \frac{\partial \psi_e\left(\mathbf{E}_e, \mathbf{K}_e\right)}{\mathbf{K}_e} = \mathbf{D} \dot{:} \mathbf{K}_e \tag{4.12}$$

This delivers the residual dissipation as the following inequality

$$\Phi = \left(\boldsymbol{\Sigma} - \boldsymbol{\Sigma}_g\right) : \overline{\mathbf{D}}_{1g} + \left(\boldsymbol{\Sigma}^{\mathbf{S}} - \boldsymbol{\Sigma}_g^{\mathbf{S}}\right) \dot{:} \overline{\mathbf{D}}_{2g} \geq 0 \tag{4.13}$$

involving the internal stresses

$$\boldsymbol{\Sigma}_g := \frac{\partial \psi_g\left(\mathbf{E}_g, \mathbf{K}_g\right)}{\mathbf{E}_g}, \ \boldsymbol{\Sigma}_g^{\mathbf{S}} := \frac{\partial \psi_g\left(\mathbf{E}_g, \mathbf{K}_g\right)}{\mathbf{K}_g}.$$

Adopting next a small strain rates framework that proves realistic for bone, it holds

$$\overline{\mathbf{D}}_{1g} = \dot{\overline{\boldsymbol{\varepsilon}}}_{1g}, \ \overline{\mathbf{D}}_{2g} = \dot{\overline{\boldsymbol{\varepsilon}}}_{2g}, \ \mathbf{E}_g := \overline{\boldsymbol{\varepsilon}}_{1g}, \ \mathbf{k}_g := \overline{\boldsymbol{\varepsilon}}_{2g}$$

We further define the thermodynamic driving forces for growth at first and second orders successively as the second- and third-order tensors

$$\mathbf{X}_{1g} := \frac{\partial \psi_g\left(\overline{\boldsymbol{\varepsilon}_{1g}}, \overline{\boldsymbol{\varepsilon}_{2g}}\right)}{\partial \overline{\boldsymbol{\varepsilon}_{1g}}}; \ \mathbf{X}_{2g} := \frac{\partial \psi_g\left(\overline{\boldsymbol{\varepsilon}_{1g}}, \overline{\boldsymbol{\varepsilon}_{2g}}\right)}{\partial \overline{\boldsymbol{\varepsilon}_{2g}}} \tag{4.14}$$

The general writing of the present growth model in tensor format shall a priori incorporate a combination of isotropic and kinematic contributions. Let define the nonnegative scalar $\overline{p}_{1g} := \int_0^t \left(\frac{2}{3}\overline{\mathbf{D}}_{1g} : \overline{\mathbf{D}}_{1g}\right)^{1/2} \mathrm{d}t$, $\overline{p}_{g2} = \int_0^t \left(\frac{1}{2}\overline{\mathbf{D}}_{2g} \dot{:} \overline{\mathbf{D}}_{2g}\right)^{1/2} \mathrm{d}t$ as the cumulative growth strain. The growth part of the free energy density is set as $\psi_g = \psi_g\left(\mathbf{E}_g := \overline{\boldsymbol{\varepsilon}}_{1g}, \mathbf{k}_g := \overline{\boldsymbol{\varepsilon}}_{2g}, \mathrm{r_g}\right)$, in which the scalar variable $\mathrm{r_g}$ is the isotropic growth hardening or softening variable, which shall have the ability to account for a possible growth recovery, given versus the effective plastic strain rate as

$$\dot{\mathrm{r}}_g = \frac{\partial \Omega}{\partial \mathrm{R_g}} = \dot{\overline{\mathrm{p}}}_g \tag{4.15}$$

Considering in the sequel a small strain rates framework which is realistic considering bone, the thermodynamic variables conjugated to the introduced internal variables $\left(\mathbf{E}_g := \overline{\boldsymbol{\varepsilon}}_{1g},\ \mathbf{k}_g = \mathbf{E}_{2g} := \overline{\boldsymbol{\varepsilon}}_{2g}, r_g\right)$ are the radius R_g representing the size of the dissipation equipotential and the center of the growth domain (conjugated to r_g) and the second- and third-order tensors $\mathbf{X}_{1g},\ \mathbf{X}_{2g}$, elaborated as the following partial derivatives:

$$R_g = \frac{\partial \psi_g\left(\mathbf{E}_g, \mathbf{E}_{2g}, r_g\right)}{\partial r_g}, \mathbf{X}_{1g} := \frac{\partial \psi_g\left(\mathbf{E}_g, \mathbf{E}_{2g}, r_g\right)}{\partial \mathbf{E}_g},\ \mathbf{X}_{2g} := \frac{\partial \psi_g\left(\mathbf{E}_g, \mathbf{E}_{2g}, r_g\right)}{\partial \mathbf{E}_{2g}} \tag{4.16}$$

These variables successively represent the size and position of the growth domain.

The local dissipation incorporating these driving forces is then obtained following the standard procedure [33] as

$$\Phi = \left(\boldsymbol{\Sigma} - \mathbf{X}_{1g}\right) : \dot{\mathbf{E}}_g + \left(\boldsymbol{\Sigma}^{\mathbf{S}} - \mathbf{X}_{2g}\right) \vdots \dot{\mathbf{E}}_{2g} - R_g \dot{r}_g \geq 0 \tag{4.17}$$

The dissipation potential is next formally introduced in stress space as

$$\varphi^* = \Omega\left(\Sigma_{eq}\left(\boldsymbol{\Sigma} - \mathbf{X}_{1g},\ \boldsymbol{\Sigma}^{\mathbf{S}} - \mathbf{X}_{2g}\right) - R_g - \sigma_g\right) \equiv \Sigma_{eq}\left(\boldsymbol{\Sigma} - \mathbf{X}_{1g},\ \boldsymbol{\Sigma}^{\mathbf{S}} - \mathbf{X}_{2g}\right) - R_g - \Sigma_g \tag{4.18}$$

In (4.18), we have introduced a possible dependency of the dissipation potential (thus of the growth process) on the hydrostatic part of the stress, which shall be tested numerically thereafter. The scalar quantity Σ_g introduced in (4.18) is the growth threshold corresponding to the minimal effective stress below which no remodeling occurs, corresponding to the lazy zone. The contributions $\Sigma_{eq}\left(\boldsymbol{\Sigma} - \mathbf{X}_{1g}\right) - R_g$ and $\mathbf{X}_{1g}$ account successively for isotropic and kinematic growth hardening. The superscript 'D' in previous and subsequent relations denotes the deviator part of the corresponding tensor, elaborated in the present 2D context from the decomposition of any second-order tensor (2.4). The first- and second-order tensors $\mathbf{X}_{1g},\ \mathbf{X}_{2g}$ are the center of the actual equipotential surface in stress and hyperstress spaces, respectively, accounting for a possible kinematic growth hardening.

Isotropic growth hardening means that the radius of the equipotential surface changes, whereas its center is fixed; kinematic growth hardening means that the radius is fixed, whereas the center is moving.

We select the following linear combination of the two invariants in the definition of the effective stress

$$\Sigma_{eq} := \left\{\alpha J_1\left(\boldsymbol{\Sigma} - \mathbf{X}_{1g}\right) + \beta J_2\left(\boldsymbol{\Sigma} - \mathbf{X}_{1g}\right) + \gamma J_1\left(\boldsymbol{\Sigma}^{\mathbf{S}} - \mathbf{X}_{2g}\right) + \delta J_2\left(\boldsymbol{\Sigma}^{\mathbf{S}} - \mathbf{X}_{2g}\right)\right\}^{1/2} \tag{4.19}$$

The equivalent stress is defined in (4.19) as the nonnegative scalar incorporating both the stress and hyperstress tensors through the first and second invariants of the differences $\left(\boldsymbol{\Sigma} - \mathbf{X}_{1g}\right),\ \left(\boldsymbol{\Sigma}^{\mathbf{S}} - \mathbf{X}_{2g}\right)$, respectively, the scalar quantities

$$\begin{aligned}
&J_1\left(\boldsymbol{\Sigma} - \mathbf{X}_{1g}\right) = Tr\left(\boldsymbol{\Sigma} - \mathbf{X}_{1g}\right), \\
&\mathrm{J}_2\left(\boldsymbol{\Sigma} - \mathbf{X}_{1g}\right) = \left(\tfrac{3}{2}\left(\boldsymbol{\Sigma} - \mathbf{X}_{1g}\right)^D : \left(\boldsymbol{\Sigma} - \mathbf{X}_{1g}\right)^D\right)^{1/2} \\
&J_1\left(\boldsymbol{\Sigma}^{\mathbf{S}} - \mathbf{X}_{2g}\right) = \left(V_i^{\nabla str}\left(\boldsymbol{\Sigma}^{\mathbf{S}} - \mathbf{X}_{2g}\right).V_i^{\nabla str}\left(\boldsymbol{\Sigma}^{\mathbf{S}} - \mathbf{X}_{2g}\right) + V_i^{rot}\left(\boldsymbol{\Sigma}^{\mathbf{S}} - \mathbf{X}_{2g}\right).V_i^{rot}\left(\boldsymbol{\Sigma}^{S} - \mathbf{X}_{2g}\right)\right)^{1/2} \\
&\mathrm{J}_2\left(\boldsymbol{\Sigma}^{\mathbf{S}} - \mathbf{X}_{2g}\right) = \left(\tfrac{1}{2}\left(\boldsymbol{\Sigma}^{\mathbf{S}} - \mathbf{X}_{2g}\right)^D \vdots \left(\boldsymbol{\Sigma}^{\mathbf{S}} - \mathbf{X}_{2g}\right)^D\right)^{1/2}
\end{aligned} \tag{4.20}$$

The first invariant of a third-order tensor is constructed from its non-deviator parts, so that $V_i^{\nabla str}$, V_i^{rot} denote here the vector parts of the harmonic decomposition of the third-order tensor $\left(\boldsymbol{\Sigma}^{\mathbf{S}} - \mathbf{X}_{2g}\right)$.

In the elaboration of the second invariant of third-order tensors, we rely on the previously established harmonic decomposition (2.7), (2.17), so that the deviator $\left(\boldsymbol{\Sigma}^{\mathbf{S}} - \mathbf{X}_{2g}\right)^D$ includes the following independent components (as summarized at the end of Sect. 2.1):

$$H_{111}\left(\left(\boldsymbol{\Sigma}^{\mathbf{S}} - \mathbf{X}_{2g}\right)_{(ijk)}\right) = \left(2\left(\boldsymbol{\Sigma}^{\mathbf{S}} - \mathbf{X}_{2g}\right)_{111} - 3\left(\boldsymbol{\Sigma}^{\mathbf{S}} - \mathbf{X}_{2g}\right)_{122}\right)$$

and

$$H_{222}\left(\left(\boldsymbol{\Sigma}^{\mathbf{S}}-\mathbf{X}_{2g}\right)_{(ijk)}\right)=\left(2\left(\boldsymbol{\Sigma}^{\mathbf{S}}-\mathbf{X}_{2g}\right)_{222}-3\left(\boldsymbol{\Sigma}^{\mathbf{S}}-\mathbf{X}_{2g}\right)_{112}\right)$$

The introduced definition of the second stress invariants $\mathrm{J}_2\left(\boldsymbol{\Sigma}-\mathbf{X}_{1g}\right)$, $\mathrm{J}_2(\boldsymbol{\Sigma}^{\mathbf{S}}-\mathbf{X}_{2g})$ is such that it delivers the expression of the uniaxial component in a pure tensile test. The growth model is then elaborated from a growth potential $\Omega_{\mathrm{g}}(f)$, a scalar-valued function of the driving force of von Mises type depending on the two parameters K, n, leading to the dissipation potential φ^*:

$$\begin{aligned}\Omega_{\mathrm{g}}(\mathrm{f}) &:= \frac{\mathrm{K}}{\mathrm{n}+1}\left(\frac{\mathrm{f}}{\mathrm{K}}\right)^{\mathrm{n}+1} \rightarrow \varphi^* = \Omega_{\mathrm{g}}\left(\Sigma_{\mathrm{eq}}\left(\boldsymbol{\Sigma}-\mathbf{X}_{1\mathrm{g}},\boldsymbol{\Sigma}^{\mathbf{S}}-\mathbf{X}_{2\mathrm{g}}\right)-\mathrm{R}_{\mathrm{g}}-\Sigma_{\mathrm{g}}\right)\\ &:= \frac{\mathrm{K}}{\mathrm{n}+1}\left(\frac{\Sigma_{\mathrm{eq}}-\mathbf{R}_{\mathrm{g}}-\Sigma_{\mathrm{g}}}{\mathrm{K}}\right)^{\mathrm{n}+1}\end{aligned} \tag{4.21}$$

The previous writing of the growth potential function representing a set of imbricate growth surfaces entails the relation linking the average first and second gradient rate of growth tensor to the conjugated driving force appearing in the local dissipation, inequality (4.7). The strength of the growth process can be accordingly be quantified by the value of the scalar growth potential Ω_{g}, low values corresponding to slow growth process, the growth velocity increasing with the value of Ω_{g} up to a rate independent growth process for very high values of the first and second gradient growth rates.

Based on the effective homogenized kinematics elaborated in Sect. 2 and the first part of Sect. 4, we search for a relation between the average rate of growth tensor and the mesoscopic driving forces, namely the applied stress tensor $\boldsymbol{\Sigma}$, to the representative volume element of bone in the form of the decoupled (due to the assumption of a centrosymmetric unit cell) functional dependency

$$\overline{\mathbf{D}}_{1\mathrm{g}}=\overline{\dot{\boldsymbol{\varepsilon}}}_{1\mathrm{g}}=\mathbf{h}_1\left(\boldsymbol{\Sigma}^{\mathrm{ext}}\right),\ \overline{\mathbf{D}}_{2\mathrm{g}}=\overline{\dot{\boldsymbol{\varepsilon}}}_{2\mathrm{g}}=\mathbf{h}_2\left(\boldsymbol{\Sigma}^{\mathbf{S},\mathrm{ext}}\right) \tag{4.22}$$

in which the two tensor-valued functions of the stress and hyperstress tensors $\mathbf{h}_1\left(\boldsymbol{\Sigma}^{\mathrm{ext}}\right),\mathbf{h}_2\left(\boldsymbol{\Sigma}^{\mathbf{S},\mathrm{ext}}\right)$ shall be elaborated later on in this contribution. The effective density shall not appear as a parameter since our model will be constructed based on real bone samples for which the density is nearly constant.

The first and second gradient average growth rate tensors are obtained from the viscoplastic type dissipation potential φ^* based on the normality rule as follows:

$$\begin{aligned}&\overline{\mathbf{D}}_{1g}=\frac{\partial\varphi^*\left(\boldsymbol{\Sigma},\mathbf{X}_{1g},R_{1g},\boldsymbol{\Sigma}^{\mathbf{S}},\mathbf{X}_{2g},R_{2g}\right)}{\partial\boldsymbol{\Sigma}}=\frac{\partial\varphi^*\left(\boldsymbol{\Sigma},\mathbf{X}_{1g},R_{1g},\boldsymbol{\Sigma}^{\mathbf{S}},\mathbf{X}_{2g},R_{2g}\right)}{\partial\Sigma_{eq}}\frac{\partial\Sigma_{eq}}{\partial\boldsymbol{\Sigma}},\\ &\frac{\partial\Sigma_{eq}}{\partial\boldsymbol{\Sigma}}=\frac{\partial\Sigma_{eq}}{\partial J_1(\boldsymbol{\Sigma}-\mathbf{X}_{1g})}\frac{\partial J_1(\boldsymbol{\Sigma}-\mathbf{X}_{1g})}{\partial\boldsymbol{\Sigma}}+\frac{\partial\Sigma_{eq}}{\partial J_2(\boldsymbol{\Sigma}-\mathbf{X}_{1g})}\frac{\partial J_2(\boldsymbol{\Sigma}-\mathbf{X}_{1g})}{\partial\boldsymbol{\Sigma}}=\left\{\alpha\mathbf{I}+\frac{3}{2}\beta\frac{(\boldsymbol{\Sigma}-\mathbf{X}_{1g})^D}{J_2(\boldsymbol{\Sigma}-\mathbf{X}_{1g})}\right\}\Big/\Sigma_{eq}\\ &\Rightarrow\overline{\mathbf{D}}_{1g}=\overline{\dot{p}}_{1g}\left\{\alpha J_1\left(\boldsymbol{\Sigma}-\mathbf{X}_{1g}\right)\mathbf{I}+\frac{3}{2}\beta\frac{(\boldsymbol{\Sigma}-\mathbf{X}_{1g})^D}{J_2(\boldsymbol{\Sigma}-\mathbf{X}_{1g})}\right\}\Big/\Sigma_{eq},\\ &\overline{\mathbf{D}}_{2g}=\frac{\partial\varphi^*\left(\boldsymbol{\Sigma},\mathbf{X}_{1g},R_g,\boldsymbol{\Sigma}^{\mathbf{S}},\mathbf{X}_{2g},R_{2g}\right)}{\partial\boldsymbol{\Sigma}^{\mathbf{S}}}=\frac{\partial\varphi^*\left(\boldsymbol{\Sigma},\mathbf{X}_{1g},R_{1g},\boldsymbol{\Sigma}^{\mathbf{S}},\mathbf{X}_{2g},R_{2g}\right)}{\partial\Sigma_{eq}}\frac{\partial\Sigma_{eq}}{\partial\boldsymbol{\Sigma}^{\mathbf{S}}}=\overline{\dot{p}}_{2g}\left\{\gamma\mathbf{I}+\frac{1}{2}\delta\frac{(\boldsymbol{\Sigma}^{\mathbf{S}}-\mathbf{X}_{2g})^D}{J_2(\boldsymbol{\Sigma}^{\mathbf{S}}-\mathbf{X}_{2g})}\right\}\Big/\Sigma_{eq}\end{aligned} \tag{4.23}$$

In previous derivations, we have accounted for the relations:

$$\begin{aligned}&\frac{\partial J_1(\boldsymbol{\Sigma}-\mathbf{X}_{1g})}{\partial\boldsymbol{\Sigma}}=\mathbf{I},\ \frac{\partial J_2(\boldsymbol{\Sigma}-\mathbf{X}_{1g})}{\partial\boldsymbol{\Sigma}}=\frac{3}{2}\frac{(\boldsymbol{\Sigma}-\mathbf{X}_{1g})^D}{J_2(\boldsymbol{\Sigma}-\mathbf{X}_{1g})}\\ &\frac{\partial J_1(\boldsymbol{\Sigma}-\mathbf{X}_{1g})}{\partial\boldsymbol{\Sigma}^{\mathbf{S}}}=\mathbf{0},\ \frac{\partial J_1(\boldsymbol{\Sigma}^{\mathbf{S}}-\mathbf{X}_{2g})}{\partial\boldsymbol{\Sigma}^{\mathbf{S}}}=\mathbf{I},\ \frac{\partial J_2(\boldsymbol{\Sigma}^{\mathbf{S}}-\mathbf{X}_{2g})}{\partial\boldsymbol{\Sigma}^{\mathbf{S}}}=\frac{1}{2}\frac{(\boldsymbol{\Sigma}^{\mathbf{S}}-\mathbf{X}_{2g})^D}{J_2(\boldsymbol{\Sigma}^{\mathbf{S}}-\mathbf{X}_{2g})}\\ &\frac{\partial\Sigma_{eq}}{\partial\boldsymbol{\Sigma}^{\mathbf{S}}}=\frac{\partial\Sigma_{eq}}{\partial J_2(\boldsymbol{\Sigma}^{\mathbf{S}}-\mathbf{X}_{2g})}\frac{\partial J_2(\boldsymbol{\Sigma}^{\mathbf{S}}-\mathbf{X}_{2g})}{\partial\boldsymbol{\Sigma}^{\mathbf{S}}}=\frac{1}{2}\delta\frac{(\boldsymbol{\Sigma}^{\mathbf{S}}-\mathbf{X}_{2g})^D}{J_2(\boldsymbol{\Sigma}^{\mathbf{S}}-\mathbf{X}_{2g})\Sigma_{eq}}\end{aligned} \tag{4.24}$$

The scalar quantity $\frac{\partial\Omega(\boldsymbol{\Sigma}^{\mathbf{s}},\mathbf{X}_{2g}R_g)}{\partial\Sigma_{eq}}$involved in (4.14) has been evaluated as follows:

$$\frac{1}{2}\overline{\mathbf{D}}_{2g}:\overline{\mathbf{D}}_{2g}=\left\{\frac{\partial\Omega\left(\boldsymbol{\Sigma}^{\mathbf{s}},\mathbf{X}_{2g}R_g\right)}{\partial\Sigma_{eq}}\right\}^2 \tag{4.25}$$

This entails that the effective growth strain rate receives the following expression:

$$\dot{\bar{p}}_{2g} := \left(\frac{1}{2}\overline{\mathbf{D}}_{2g} : \overline{\mathbf{D}}_{2g}\right)^{1/2} = \frac{\partial \Omega\left(\boldsymbol{\Sigma}^{\mathbf{s}}, \mathbf{X}_{2g} R_g\right)}{\partial \Sigma_{eq}} \tag{4.26}$$

The internal variables $(\boldsymbol{\alpha}_g, r_g)$ associated with the driving forces $\mathbf{X}_g$, R_g are then given by the following normality rule:

$$\begin{aligned}
\dot{\boldsymbol{\alpha}}_{1g} &= -\frac{\partial \Omega(\boldsymbol{\Sigma}, \mathbf{X}_{1g}, \boldsymbol{\Sigma}^{\mathbf{s}}, \mathbf{X}_{2g}, R_g)}{\partial \mathbf{X}_{1g}} = \frac{\partial \Omega(\boldsymbol{\Sigma}, \mathbf{X}_{1g}, \boldsymbol{\Sigma}^{\mathbf{s}}, \mathbf{X}_{2g}, R_g)}{\partial \boldsymbol{\Sigma}}, \\
\dot{\boldsymbol{\alpha}}_{2g} &= -\frac{\partial \Omega(\boldsymbol{\Sigma}, \mathbf{X}_{1g}, \boldsymbol{\Sigma}^{\mathbf{s}}, \mathbf{X}_{2g}, R_g)}{\partial \mathbf{X}_{2g}} = \frac{\partial \Omega(\boldsymbol{\Sigma}, \mathbf{X}_{1g}, \boldsymbol{\Sigma}^{\mathbf{s}}, \mathbf{X}_{2g}, R_g)}{\partial \boldsymbol{\Sigma}^{\mathbf{s}}}, \\
\dot{r}_g &= -\frac{\partial \Omega(\boldsymbol{\Sigma}, \mathbf{X}_{1g}, \boldsymbol{\Sigma}^{\mathbf{s}}, \mathbf{X}_{2g}, R_g)}{\partial R_g} = \frac{\partial \Omega(\boldsymbol{\Sigma}, \mathbf{X}_{1g}, \boldsymbol{\Sigma}^{\mathbf{s}}, \mathbf{X}_{2g}, R_g)}{\partial \Sigma_{eq}}
\end{aligned} \tag{4.27}$$

These equalities obtained by considering the specific form of the dissipation potential in (4.21) (tensors $\boldsymbol{\Sigma}$, $\boldsymbol{\Sigma}^{\mathbf{S}}$, $\mathbf{X}_{1g}$, $\mathbf{X}_{2g}$ intervene through their difference, and similarly for quantities Σ_{eq} and R_g) ensure the positive nature of the local dissipation, inequality (4.17).

We shall in the sequel consider a perfect viscoplastic model without isotropic hardening. Time is indeed in the present model not a physical parameter influencing directly growth, but instead the applied stress (or displacement) over the RUC dictates the growth rate, and there is no time hardening. We accordingly neglect isotropic hardening (in coherence with viscoplastic models neglecting primary creep, [33]), since the microscopic external remodeling law (3.8) entails that growth develops at constant applied stress, provided the effective stress is located outside the lazy zone described by the scalar parameter Σ_g. The average growth model can accordingly be considered as a pure viscoplastic model in which growth hardening can be discarded. In the next section, we shall identify the effective first- and second-order moduli of the considered 2D trabecular bone sample (Fig. 1b) at both initial and growth conditions.

5 Determination of homogenized first and second gradient stiffness tensors for the initial and grown trabecular bone

5.1 Basic equations and constitutive relations

In classical elasticity theory, only the first displacement gradient is involved and all the higher-order displacement gradients are neglected in measuring the deformations. In this situation, the stress at a material point is linked to strain through the classical elasticity tensor. The strain gradient elasticity is a kinematic enhancement of classical elasticity taking into account the second gradient of deformation in the mechanical formulation. In this case, the constitutive law provides the symmetric Cauchy stress tensor $\boldsymbol{\Sigma}$ and the hyperstress tensor $\boldsymbol{\Sigma}^{\mathbf{S}}$. In the case where the microstructure of a material exhibits central symmetry, the first- and second-order tensors $\boldsymbol{\Sigma}$ and $\boldsymbol{\Sigma}^{\mathbf{S}}$ are related to $\boldsymbol{\varepsilon} = \frac{1}{2}\left(\boldsymbol{u} \otimes \nabla + \boldsymbol{u} \otimes \nabla^{\mathrm{T}}\right)$ and $\mathbf{k} = \boldsymbol{\varepsilon} \otimes \nabla$ through the following general constitutive law for a homogeneous second-order grade continuum written successively in tensor format and with index notation:

$$\begin{aligned}
\boldsymbol{\Sigma} = \mathbf{C} : \boldsymbol{\varepsilon} \;&\Leftrightarrow\; \Sigma_{ij} = C_{ijkl}\varepsilon_{kl} \\
\boldsymbol{\Sigma}^{\mathbf{S}} = \mathbf{D} \dot{:} \mathbf{k} \;&\Leftrightarrow\; \Sigma^{S}_{ijk} = D_{ijklmn}k_{lmn}
\end{aligned} \tag{5.1}$$

with C_{ijlm} the classical fourth-order elastic tensor and D_{ijklmn} the sixth-order second stiffness elastic tensor (their components).

In two dimensions (2D), the displacement field writes as the vector $\boldsymbol{u} = \left[u_x, u_y\right]^{\mathrm{T}}$, which entails the following strain tensor in vector form

$$\boldsymbol{\varepsilon} = \left[\varepsilon_{xx} = \boldsymbol{u}_{x,x}, \varepsilon_{yy} = \boldsymbol{u}_{y,y}, \varepsilon_{xy} = \varepsilon_{yx} = \frac{1}{2}\left(\boldsymbol{u}_{\mathrm{y},x} + \boldsymbol{u}_{x,\mathrm{y}}\right)\right]^{\mathrm{T}} \tag{5.2}$$

In the same way, the strain gradient field determines a tensor with the following six independent components represented in vector format accounting for its index symmetries as

$$k = \left[\varepsilon_{\mathrm{xx,x}}, \varepsilon_{\mathrm{yy,y}}, \varepsilon_{\mathrm{xx,y}}, \varepsilon_{\mathrm{yy,x}}, \varepsilon_{\mathrm{xy,x}}, \varepsilon_{\mathrm{xy,y}}\right]^{\mathrm{T}} = \left[\mathrm{u}_{\mathrm{x,xx}}, \mathrm{u}_{\mathrm{y,yy}}, \mathrm{u}_{\mathrm{x,xy}}, \mathrm{u}_{\mathrm{y,xy}}, \frac{1}{2}\left(\mathrm{u}_{\mathrm{y,xx}} + \mathrm{u}_{\mathrm{x,xy}}\right), \frac{1}{2}\left(\mathrm{u}_{\mathrm{y,xy}} + \mathrm{u}_{\mathrm{x,yy}}\right)\right]^{\mathrm{T}} \tag{5.3}$$

The stress and hyperstress for the effective 2D strain gradient continuum can be defined as

$$\boldsymbol{\Sigma} = \left[\Sigma_{xx}, \Sigma_{yy}, \Sigma_{xy}\right]^{\mathrm{T}}, \boldsymbol{\Sigma}^{\mathbf{S}} = \left[\Sigma^{S}_{xxx}, \Sigma^{S}_{yyy}, \Sigma^{S}_{xxy}, \Sigma^{S}_{yxy}, \Sigma^{S}_{yxx}, \Sigma^{S}_{xyy}\right]^{\mathrm{T}} \tag{5.4}$$

The effective first- and second-order elastic moduli are identified for the growing bone tissue at the mesoscopic level in the next section.

5.2 Identification of the first and second equivalent elastic moduli for the initial and grown trabecular microstructures

This section aims at the determination of the effective constitutive coefficients of the strain gradient continuum from the RVE response of trabecular bone network. We design different boundary conditions for the determination of the components of the constitutive (rigidity) constants over the RVE sample (Fig. 1b) with boundary $\partial\Omega$. In each case, we force the RVE in the present 2D context to bear the designed specific deformations $\boldsymbol{\varepsilon} = \left[\varepsilon_{xx}, \varepsilon_{yy}, \varepsilon_{xy}\right]$, $\boldsymbol{k} = \left[k_{xxx}, k_{yyy}, k_{xxy}, k_{yxy}, k_{yxx}, k_{xyy}\right]$ and compute numerically the total elastic strain energy U_{RVE} stored in the unit cell under the corresponding boundary conditions. For more details, the reader is referred to Goda and Ganghoffer [24].
The numerical procedure used here to identify the first- and second-order gradient elastic moduli is as follows: The total strain energy stored in the RVE is equated with the energy of an equivalent homogeneous strain gradient continuum; thus,

$$U_{RVE} = U_{strain\ gradient} = \frac{V_{RVE}}{2}\left[\varepsilon_{ij} C_{ijkl} \varepsilon_{kl} + k_{ijk} D_{ijklmn} k_{lmn}\right] \tag{5.5}$$

where $V_{RVE} = |\Omega|$ is the volume of the RVE. The left-hand side in (5.5) is the total elastic strain energy stored in the RVE, while the right-hand side is the expression of the energy of the postulated effective strain gradient continuum.
In order to evaluate the components of the first- and second- gradient elasticity stiffness tensors $\mathbf{C}$ and $\mathbf{D}$ for the underlying RVE of trabecular bone, we conduct a set of ten elementary tests described in Appendix.

It is convenient to summarize the set of equations of the field variables concerning the first and second gradient static and growth scheme. Box 1 illustrates the equations corresponding to equilibrium at the surface and in the bulk, the surface constitutive law, the surface density, the surface growth model, and the definition of the homogenized static model for the initial and grown structure based on strain gradient. Based on this, Box 2 exposes the definition of the first- and second-order average kinematics, the effective growth strain and strain gradient rate, and the constitutive model for the growing bone structure.
Accounting for both first and second-order deformation gradients, simulations for the purpose of evaluating both static and growth effective properties are done over the considered trabecular bone RUC with the open-source FE software FreeFem++. These simulations are based on the weak form of the set of field equations given in Box 1 and Box 2.

In order to illustrate the application of bone adaptation in numerical computations based on strain gradient framework, bone internal and external remodeling at trabecular level is predicted, starting from an initial geometry with a uniform density distribution of 1500 kg/m^3. The local distributions of the equivalent strain (a scalar measure of the strain tensor) in the considered trabecular bone sample are illustrated in Fig. 3a, b for the load cases corresponding to first gradient of displacement (uniaxial extension, shear), and in Fig. 4a–f for the load cases corresponding to the strain gradient with components

$$k_{xxx} = \varepsilon_{xx,x}, k_{yyy} = \varepsilon_{yy,y}, k_{xxy} = \varepsilon_{xx,y}, k_{yxy} = \varepsilon_{yy,x}, k_{yxx} = \varepsilon_{xy,x}, k_{xyy} = \varepsilon_{xy,y}.$$

As a general trend, we observe from Figs. 3 and 4 that high surface strains give locally rise to significant bone growth (formation). For any load applied to the trabecular structure whether the first or second gradient of displacement, local strains in the surfaces become very high at the conjunction of the trabeculae. These strains in turn stimulate bone formation that occurs mainly along the trabecular edges. Therefore, we conclude that bone growth most likely occurs at sites of high mechanical strain.
The equivalent first and second gradient stiffness tensors $\mathbf{C}$ and $\mathbf{D}$ coefficients (Tables 1 and 2) have been computed at the initial state when growth has not yet occurred. We notice that the RUC is not completely isotropic; the identified initial first- and second-order stiffness components C_{11} and D_{111} are slightly different than C_{22} and D_{222}, reflecting the overall orthotropy of the bone microstructure.

Balance of surface momentum :

$$\begin{cases} \nabla_S.\tilde{\boldsymbol{\Sigma}}_a - \boldsymbol{\Pi}.\mathbf{K}^T.\dfrac{\partial W^S}{\partial N} + \tilde{\mathbf{F}}^T.\mathbf{f}_S = \mathbf{0} \quad \text{on } \Omega_g,\ \nabla_S = \boldsymbol{\Pi}.\nabla \\ \mathbf{f}_S = \mathbf{0} \text{ on } \Omega_g \setminus \Omega_t \end{cases}$$

Equilibrium equation for the bulk elasticity :

$$\begin{cases} \mathrm{div}\boldsymbol{\sigma} + \rho\mathbf{g} = \mathbf{0} \text{ in } \Omega \\ \boldsymbol{\Sigma}_a = W_0\mathbf{I} - \boldsymbol{\varepsilon}_a^T.\boldsymbol{\sigma} \\ \mathbf{U} = \mathbf{0} \text{ on } \Omega_u;\ \boldsymbol{\sigma}.\mathbf{N} = \mathbf{f}_S \text{ on } \Omega_t \\ \boldsymbol{\sigma} = 2\mu(\rho)\boldsymbol{\varepsilon}_a + \lambda(\rho)\mathrm{Tr}(\boldsymbol{\varepsilon}_a)\mathbf{I} \end{cases}$$

Surface constitutive law :

$$\begin{cases} W^S = \dfrac{\lambda(\rho)}{2}\mathrm{Tr}(\tilde{\boldsymbol{\varepsilon}}_a)^2 + \mu(\rho)(\tilde{\boldsymbol{\varepsilon}}_a : \tilde{\boldsymbol{\varepsilon}}_a) \\ \tilde{\boldsymbol{\Sigma}}_a = W^S\boldsymbol{\Pi} - \tilde{\boldsymbol{\varepsilon}}_a^T.\dfrac{\partial W^S}{\partial \tilde{\boldsymbol{\varepsilon}}_a} \end{cases}$$

Surface growth velocity :

$$\tilde{\mathbf{V}}_g = K\nabla_S.(\tilde{\boldsymbol{\Sigma}}_a) \quad \text{on } \Omega_g,\ \tilde{K} = \mathrm{Cte}$$

Surface density equation :

$$\dot{\rho}_g = \Gamma^S\rho_g \quad \text{on } \Omega_g$$

$$\Gamma^S = \mathrm{tr}\left(\dot{\tilde{\mathbf{F}}}_g.\tilde{\mathbf{F}}_g^{-1}\right) = \frac{\tilde{B}}{\rho_g^2}\mathrm{tr}\left(\boldsymbol{\Sigma}_a(\boldsymbol{\varepsilon}_a) - \boldsymbol{\Sigma}_0\right)$$

$$\rho_g(\mathbf{X}, t=0) = \rho_0(\mathbf{X})$$

Constitutive law for a strain gradient model :

$$\boldsymbol{\Sigma} = \mathbf{C} : \boldsymbol{\varepsilon} \quad \Leftrightarrow \Sigma_{ij} = C_{ijkl}\varepsilon_{kl}$$

$$\boldsymbol{\Sigma}^S = \mathbf{D} \vdots \mathbf{k} \quad \Leftrightarrow \Sigma^S_{ijk} = D_{ijklmn}k_{lmn}$$

Strain energy based on strain gradient model :

$$U_{RVE} = U_{\text{strain gradient}} = \frac{V_{RVE}}{2}\left[\varepsilon_{ij}C_{ijkl}\varepsilon_{kl} + k_{ijk}D_{ijklmn}k_{lmn}\right] \rightarrow C_{ijkl}, D_{ijklmn}$$

Box 1 Summary of the equations used to simulate bone remodeling along with equations to evaluate the first and second gradient equivalent elastic moduli in the static case and growth situation

Since we aim at simulating bone remodeling from the assumed initial configuration of trabecular bone RUC, the effective first and second gradient moduli are expected to evolve with the grown state of trabecular bone structure. Thus, we repeat the previous identification of the homogenized first and second gradient stiffness coefficients at different time steps associated with different grown configurations. The evolution of the effective first- and second-order rigidity components versus the remodeling time step is given in Fig. 5. It is actually observed that throughout the growth process the effective first gradient moduli (tensile and shear coefficients) increase faster than the second gradient coefficients D_{ijk}. This shows that second gradient moduli are less influenced by growth in comparison with the first gradient effective moduli.

The characteristic length is an essential parameter in the strain gradient continua. The characteristic length indicates the nature and significance of non-classical phenomena in the response of a medium with microstructure like in trabecular bone. Therefore, the characteristic lengths are next identified from the homogenized first and second gradient stiffness moduli. In 3D situation, six internal characteristic lengths associated with the independent classical moduli C_{ij} can be identified by the following relation (see [24]):

$$l_{\alpha\beta} = \left(\frac{\sum_{r=1}^{3} D_{\alpha r\beta r}}{C_{\alpha\beta}}\right)^{1/2} \tag{5.6}$$

First and second order average kinematics:

$$\begin{cases}
\overline{\mathbf{D}}_{\mathrm{l}} = \dfrac{1}{V}\displaystyle\int_{V}\mathbf{D}_{\mathrm{l}}\,dX = \dfrac{1}{|V|}\int_{\partial V}\dfrac{1}{2}\left(\mathbf{V}\otimes\mathbf{N}+\mathbf{N}\otimes\mathbf{V}\right)dS \\
\overline{\mathbf{L}}_{\mathrm{g}} := \dfrac{1}{|V|}\displaystyle\int_{\partial V_B}\mathbf{V}_{\mathrm{g}}\otimes\mathbf{N}\,dS \\
\overline{\mathbf{D}}_{\mathrm{lg}} = \dfrac{1}{2}\left(\overline{\mathbf{L}}_{\mathrm{g}}+\overline{\mathbf{L}}_{\mathrm{g}}^{\mathrm{T}}\right) = \dfrac{1}{|V|}\displaystyle\int_{\partial V_B}\dfrac{1}{2}\left(\mathbf{V}_{\mathrm{g}}\otimes\mathbf{N}+\mathbf{N}\otimes\mathbf{V}_{\mathrm{g}}\right)dS \\
\overline{\mathbf{D}}_{\mathrm{le}} = \overline{\mathbf{D}}_{\mathrm{l}} - \overline{\mathbf{D}}_{\mathrm{lg}} \\
\overline{\mathbf{K}}_{\mathrm{g}} := \dfrac{1}{|V|}\displaystyle\int_{\partial V_B}\left(\mathbf{V}_{\mathrm{g}}\otimes\nabla_{\mathrm{x}}\right)\otimes\mathbf{N}\,dS \equiv \dfrac{1}{|V|}\int_{\partial V_B}\left(\mathbf{V}_{\mathrm{g}}\otimes\nabla_{\mathrm{x}}\right)\otimes\nabla_{\mathrm{x}}\,dV \rightarrow \left(\dot{\mathrm{K}}_{\mathrm{g}}\right)_{\mathrm{ijk}} = \left(\dot{\mathrm{K}}_{\mathrm{g}}\right)_{\mathrm{ikj}} \\
\overline{\mathbf{D}}_{2\mathrm{g}} := \dfrac{1}{2}\left(\overline{\mathbf{K}}_{\mathrm{g}}+\overline{\mathbf{K}}_{\mathrm{g}}^{\mathrm{T}}\right);\quad \left(\overline{\mathrm{D}}_{2\mathrm{g}}\right)_{\mathrm{ijk}} = \left(\overline{\mathrm{D}}_{2\mathrm{g}}\right)_{\mathrm{jik}} = \left(\overline{\mathrm{D}}_{2\mathrm{g}}\right)_{\mathrm{ikj}} \\
\overline{\mathbf{D}}_{2\mathrm{e}} := \overline{\mathbf{D}}_{2} - \overline{\mathbf{D}}_{2\mathrm{g}};\quad \left(\overline{\mathrm{D}}_{2\mathrm{e}}\right)_{\mathrm{ijk}} = \left(\overline{\mathrm{D}}_{2\mathrm{e}}\right)_{\mathrm{jik}} = \left(\overline{\mathrm{D}}_{2\mathrm{e}}\right)_{\mathrm{ikj}}
\end{cases}$$

Strain gradient growth model :

$$\begin{cases}
\mathrm{J}_1\left(\boldsymbol{\Sigma}-\mathbf{X}_{1\mathrm{g}}\right) = \mathrm{Tr}\left(\boldsymbol{\Sigma}-\mathbf{X}_{1\mathrm{g}}\right) \\
\mathrm{J}_2\left(\boldsymbol{\Sigma}-\mathbf{X}_{1\mathrm{g}}\right) = \left(\dfrac{3}{2}\left(\boldsymbol{\Sigma}-\mathbf{X}_{1\mathrm{g}}\right)^{\mathrm{D}}:\left(\boldsymbol{\Sigma}-\mathbf{X}_{1\mathrm{g}}\right)^{\mathrm{D}}\right)^{1/2} \\
\mathrm{J}_1\left(\boldsymbol{\Sigma}^{\mathrm{S}}-\mathbf{X}_{2\mathrm{g}}\right) = \left(\mathrm{V}_{\mathrm{i}}^{\nabla\mathrm{str}}\left(\boldsymbol{\Sigma}^{\mathrm{S}}-\mathbf{X}_{2\mathrm{g}}\right).\mathrm{V}_{\mathrm{i}}^{\nabla\mathrm{str}}\left(\boldsymbol{\Sigma}^{\mathrm{S}}-\mathbf{X}_{2\mathrm{g}}\right)+\mathrm{V}_{\mathrm{i}}^{\mathrm{rot}}\left(\boldsymbol{\Sigma}^{\mathrm{S}}-\mathbf{X}_{2\mathrm{g}}\right).\mathrm{V}_{\mathrm{i}}^{\mathrm{rot}}\left(\boldsymbol{\Sigma}^{\mathrm{S}}-\mathbf{X}_{2\mathrm{g}}\right)\right)^{1/2} \\
\mathrm{J}_2\left(\boldsymbol{\Sigma}^{\mathrm{S}}-\mathbf{X}_{2\mathrm{g}}\right) = \left(\dfrac{1}{2}\left(\boldsymbol{\Sigma}^{\mathrm{S}}-\mathbf{X}_{2\mathrm{g}}\right)^{\mathrm{D}}:\left(\boldsymbol{\Sigma}^{\mathrm{S}}-\mathbf{X}_{2\mathrm{g}}\right)^{\mathrm{D}}\right)^{1/2} \\
\Sigma_{\mathrm{eq}} = \left\{\alpha\mathrm{J}_1\left(\boldsymbol{\Sigma}-\mathbf{X}_{1\mathrm{g}}\right)+\beta\mathrm{J}_2\left(\boldsymbol{\Sigma}-\mathbf{X}_{1\mathrm{g}}\right)+\gamma\mathrm{J}_1\left(\boldsymbol{\Sigma}^{\mathrm{S}}-\mathbf{X}_{2\mathrm{g}}\right)+\delta\mathrm{J}_2\left(\boldsymbol{\Sigma}^{\mathrm{S}}-\mathbf{X}_{2\mathrm{g}}\right)\right\}^{1/2} \\
\Omega_{\mathrm{g}} := \dfrac{\mathrm{K}}{\mathrm{n}+1}\left(\dfrac{\Sigma_{\mathrm{eq}}}{\mathrm{K}}\right)^{\mathrm{n}+1} \\
\varphi^{*} = \dfrac{\mathrm{K}}{\mathrm{n}+1}\left(\dfrac{\Sigma_{\mathrm{eq}}-\mathrm{R}_{\mathrm{g}}-\Sigma_{\mathrm{g}}}{\mathrm{K}}\right)^{\mathrm{n}+1} \\
\overline{\mathbf{D}}_{1\mathrm{g}} = \dot{\bar{\mathrm{p}}}_{1\mathrm{g}}\left\{\alpha\mathrm{J}_1\left(\boldsymbol{\Sigma}-\mathbf{X}_{1\mathrm{g}}\right)\mathbf{I}+\dfrac{3}{2}\beta\dfrac{\left(\boldsymbol{\Sigma}-\mathbf{X}_{1\mathrm{g}}\right)^{\mathrm{D}}}{\mathrm{J}_2\left(\boldsymbol{\Sigma}-\mathbf{X}_{1\mathrm{g}}\right)}\right\}/\Sigma_{\mathrm{eq}} \\
\overline{\mathbf{D}}_{2\mathrm{g}} = \dot{\bar{\mathrm{p}}}_{2\mathrm{g}}\left\{\gamma\mathbf{I}+\dfrac{1}{2}\delta\dfrac{\left(\boldsymbol{\Sigma}^{\mathrm{S}}-\mathbf{X}_{2\mathrm{g}}\right)^{\mathrm{D}}}{\mathrm{J}_2\left(\boldsymbol{\Sigma}^{\mathrm{S}}-\mathbf{X}_{2\mathrm{g}}\right)}\right\}/\Sigma_{\mathrm{eq}}
\end{cases}$$

Box 2 Summary of the equations describing the effective growth model based on the strain gradient theory

This equality follows from the major symmetry of the second gradient elasticity coefficients. The material length parameters appear as the ratio of second-order to first order equivalent moduli. Due to the present 2D context, three internal lengths associated with the independent classical moduli can then be identified by the relations

$$l_{11} = \left(\frac{D_{111}+D_{112}}{C_{11}}\right)^{1/2},\ l_{22} = \left(\frac{D_{212}+D_{222}}{C_{22}}\right)^{1/2},\ l_{12} = \left(\frac{D_{112}+D_{122}}{C_{33}}\right)^{1/2} \tag{5.7}$$

In order to assess the relevance of a strain gradient continuum model, the characteristic lengths for the strain gradient behavior, described by Eq. (5.7), are evaluated versus the remodeling time. The ratio of the characteristic internal lengths to the characteristic unit cell size, quantity L, is plotted in Fig. 6 versus the remodeling time step to assess the strength of the strain gradient effect. It appears that those ratios have of an order of magnitude close to unity, indicating that strain gradient effects indeed impact the continuum behavior.

Regarding the evolution behavior of the characteristic lengths versus the remodeling time (Fig. 6), it is actually noticed that throughout the growth process the internal lengths decrease with remodeling time; in addition, the characteristic length associated with shear deformation mode l_{12} decreases faster than the one

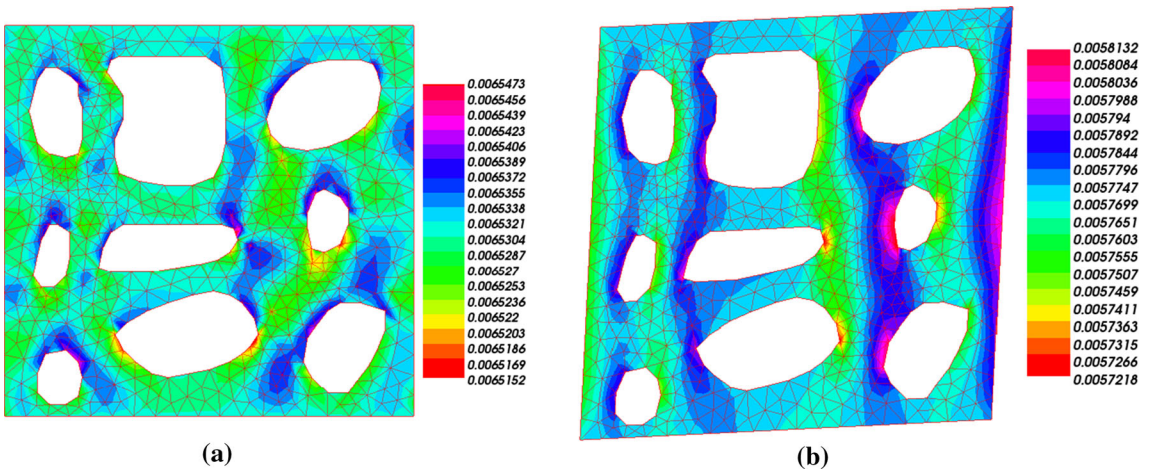

Fig. 3 Strain distributions in the RUC of trabecular bone, **a** Uniaxial tension along x and **b** Simple shear

associated with the tensile mode, scalar l_{11}. We can explain the overall decrease in the internal length with ongoing remodeling by the fact that during the growth process the effective first gradient moduli C_{ij} increase faster than the second gradient moduli D_{ijk} with remodeling time as shown previously in Fig. 5; moreover, the shear effective rigidity is increasing faster than the effective tensile rigidity, as shown in Fig. 5 (left plot).

5.3 Effective second gradient moduli of a two-phase bone structure including marrow

In order to improve our understanding of the trabecular bone effective mechanical behavior, it is interesting to determine the effects of the presence of bone marrow on the effective first and second gradient moduli of trabecular bone. This section focuses on the mechanical behavior analysis of trabecular bone at the mesoscopic scale under prescribed first- and second-order boundary conditions, paying attention to trabecular bone with bone marrow filling the porosities.

In Fig. 7, we represent trabecular bone as 2D structure, consisting of hard tissue (bone trabeculae) and soft tissue (bone marrow). To well explain the bone marrow contribution on the effective strain gradient mechanical behavior of trabecular bone at the initial and growth state, FE investigations using the FE code Freefem++ have been performed to capture the interaction between bone and marrow under various loading conditions.

We assume that both material phases are homogeneous, linear elastic, and isotropic. Bone tissue is assigned to have a Young's modulus determined from Eq. (3.11) and a Poisson ratio of 0.3, while the cavities are filled with soft material with a Young's modulus of 2 MPa and a Poisson ratio of 0.167 [31]. The calculated components of the effective initial first and second gradient stiffness tensors obtained in situations including and excluding bone marrow are summarized in Table 3.

When analyzing the numerically quantified bone marrow effects, we observe that bone marrow contributes to an overall insignificant increase in the effective initial first and second gradient mechanical properties. The maximum increase in moduli occurs for the biaxial and shearing modes, followed by the increase in the second gradient components D_{211} and D_{122}. This can be explained as the presence of bone marrow causes stiffening effect under these tests. In the situation of bone marrow effect on the effective moduli during the growth process, we observe that the first and second gradient moduli follow similar contributions by a small overall increase.

5.4 Identification of the material parameters of the constitutive law for growing bone

We search a relationship between the average rate of growth tensor and the rate of elastic deformation tensor with the applied stress and hyperstress tensors $\boldsymbol{\Sigma}^{\text{ext}}$, $\boldsymbol{\Sigma}^{\mathbf{S},\text{ext}}$, as expressed in relations (4.6). The effective stress and hyperstress are evaluated from the average strain and strain gradient imposed over the RUC simply from the computed effective moduli (the average strains and strain gradients are imposed over the RUC).

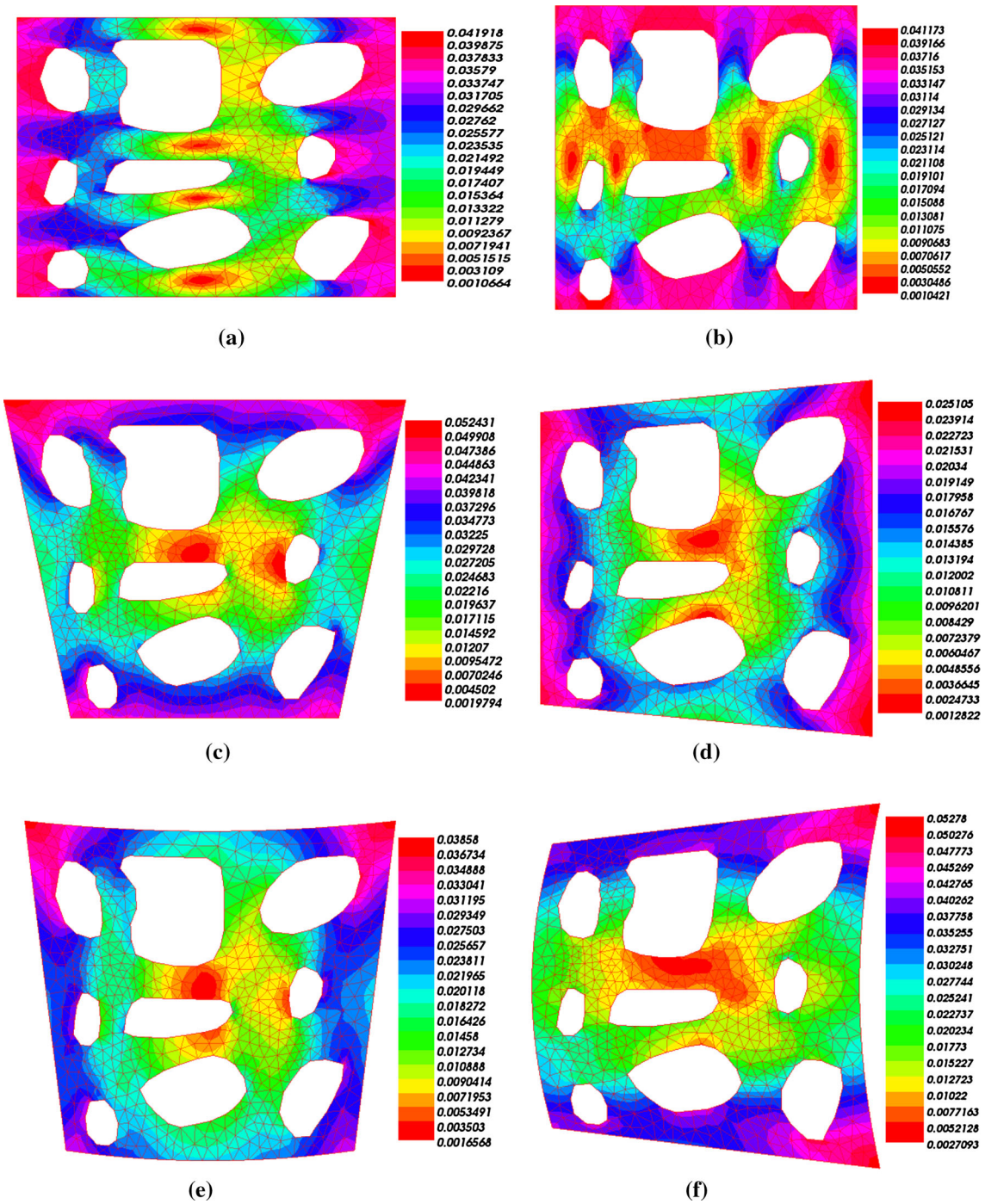

Fig. 4 Strain distributions in the RUC of trabecular bone due to the load cases corresponding to the strain gradient. **a** $k_{xxx} = \varepsilon_{xx,x}$, **b** $k_{yyy} = \varepsilon_{yy,y}$, **c** $k_{xxy} = \varepsilon_{xx,y}$, **d** $k_{yxy} = \varepsilon_{yy,x}$, **e** $k_{yxx} = \varepsilon_{xy,x}$, and **f** $k_{xyy} = \varepsilon_{xy,y}$

In order to test a possible asymmetry between traction and compression and thus the existence of a growth kinematic hardening, we record over RUC the evolution of component of the average second gradient rate of growth tensor $\left(\overline{\mathbf{D}}_{2g}\right)_{111}$ versus the corresponding hyperstress component $\mathbf{\Sigma}^{\mathbf{S}}_{111}$ in both tensile and compression simulations along direction x. The stress–strain response shows a symmetric response (Fig. 8), so one can conclude that no kinematic hardening is present; the same conclusion is reached for tensile and compressive loads applied along the x direction—the plots are, however, not shown. This find-

Table 1 Effective initial first gradient stiffness coefficients identified numerically. Unit is MPa

C11	C22	C12	C33
245.41	243.56	49.88	64.86

Table 2 Effective initial second gradient stiffness coefficients identified numerically. Units is N

D_{111}	D_{222}	D_{112}	D_{212}	D_{211}	D_{122}
915.6	1035.0	2567.8	2913.4	4068.6	4211.8

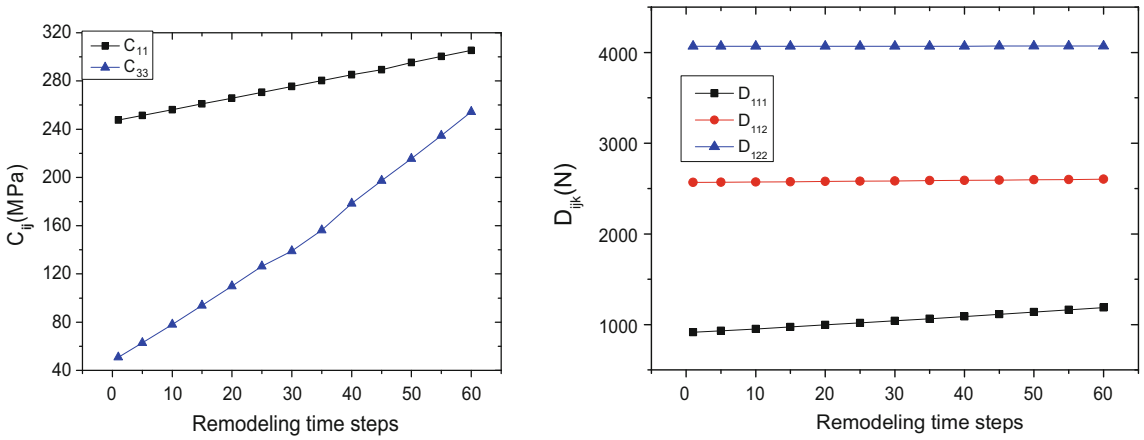

Fig. 5 First and second gradient elasticity stiffness tensors C_{ij} (left) and D_{ijk} (right) versus the remodeling time step

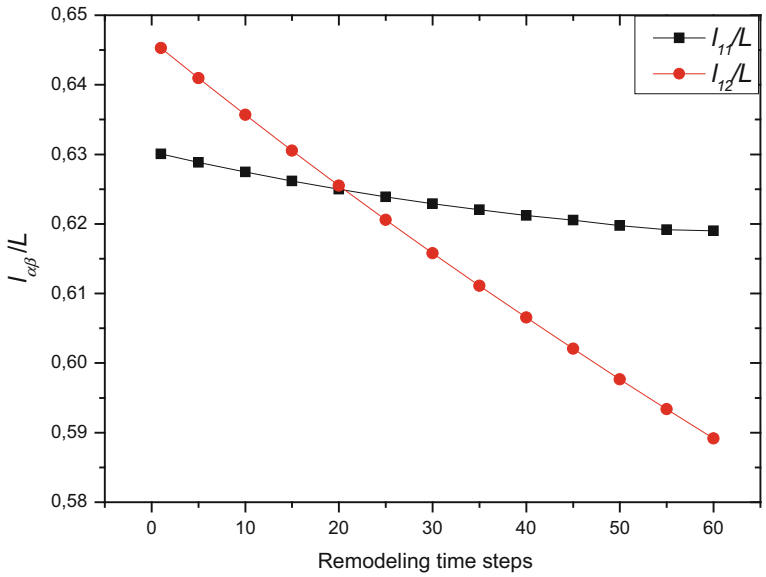

Fig. 6 Ratio of the characteristic strain gradient lengths to the unit cell size of trabecular bone versus the remodeling time step

ing extends a similar absence of kinematic hardening already observed for the first displacement gradient model [35].

Time is in the present model not a physical parameter influencing directly growth, but instead the applied stress over the RUC dictates the growth rate, and there is no time hardening. We accordingly neglect isotropic hardening (this is consistent with viscoplastic models neglecting primary creep, Lemaitre and Chaboche [33]).

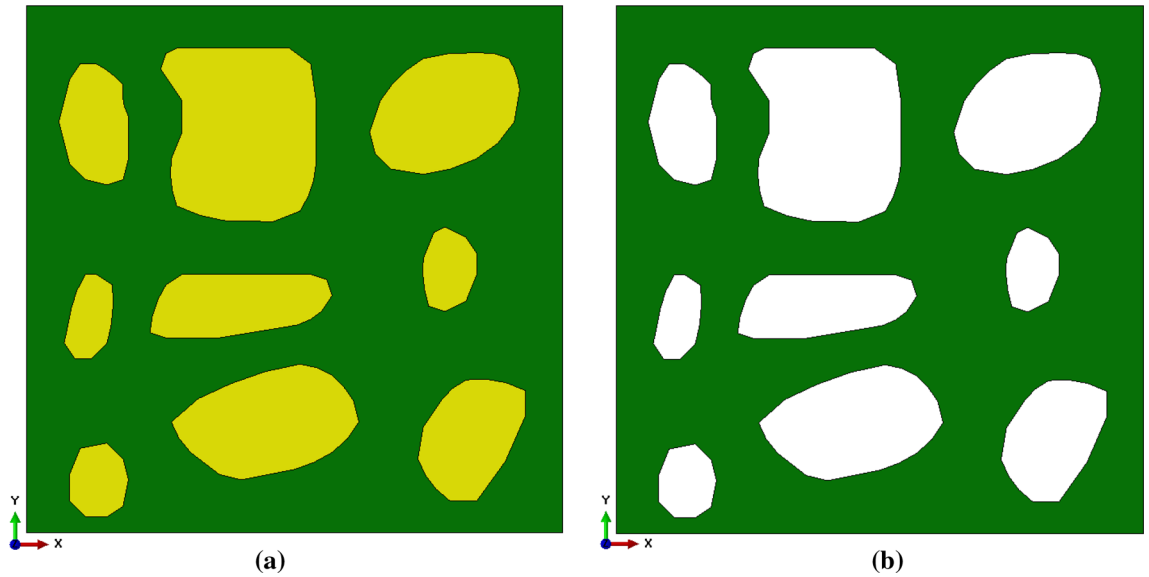

Fig. 7 Representation of trabecular bone RUC composed of bony trabecular struts and marrow-filled cavities. **a** Bone tissue with marrow and **b** bone tissue alone

Table 3 Effective initial first and second gradient moduli (Cij and Dijk) of trabecular bone RUC with and without bone marrow

C_{ij} (MPa)		C11	C22	C12	C33	
With bone marrow		247.70	245.84	50.82	66.20	
Without bone marrow		245.41	243.56	49.88	64.86	
Relative difference (%)		0.93	0.93	2	2	
D_{ijk} (N)	D_{111}	D_{222}	D_{112}	D_{212}	D_{211}	D_{122}
With bone marrow	922.3	1040.6	2585.6	2930	4102.0	4247
Without bone marrow	915.6	1035.0	2567.8	2913.4	4068.6	4211.8
Relative difference (%)	0.73	0.54	0.73	0.60	0.82	0.84

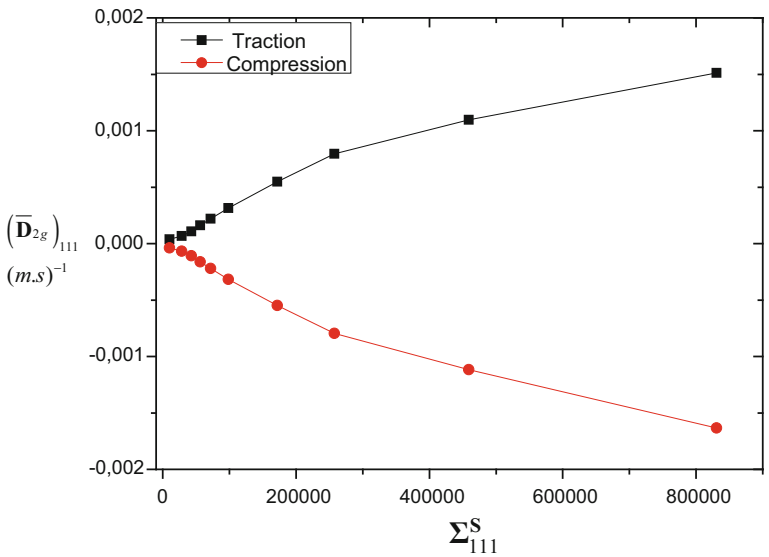

Fig. 8 Evolution of component of the average second gradient rate of growth tensor $\left(\overline{\mathbf{D}}_{2g}\right)_{111}$ versus the corresponding hyperstress component Σ^{S}_{111} under tension and compression over 60 growth time steps

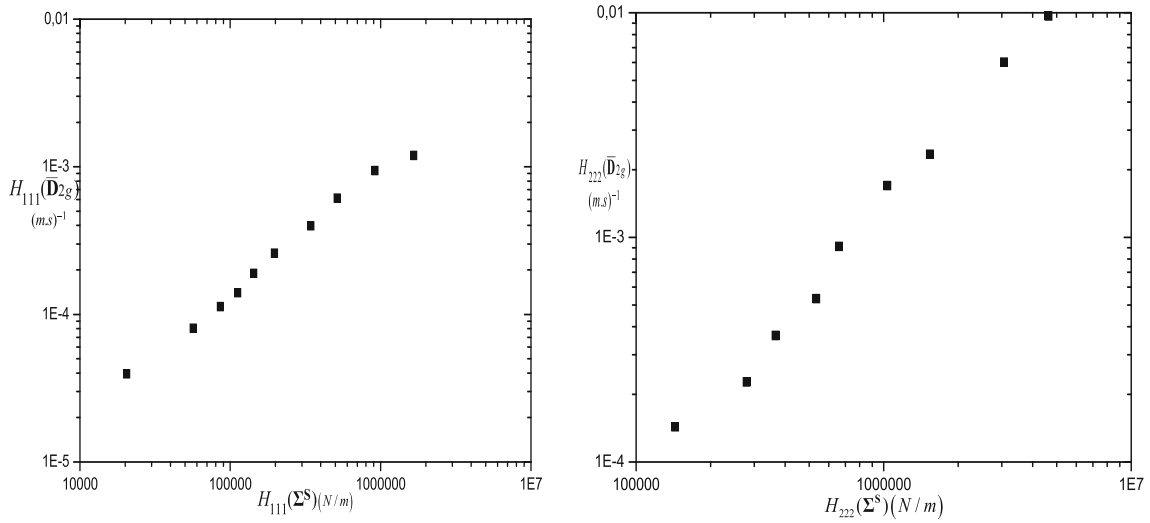

Fig. 9 Components of the third-order deviator tensor H_{ijk} of $\overline{\mathbf{D}}_{2g}$ versus the corresponding components of the hyperstress deviator

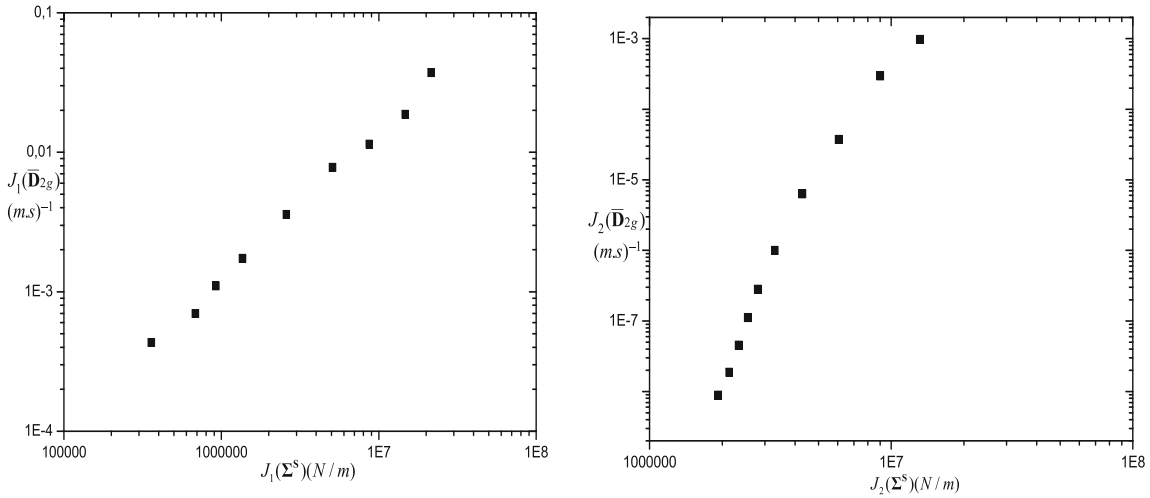

Fig. 10 First and second invariant of $\overline{\mathbf{D}}_{2g}$ versus the first and second invariants of the hyperstress tensor

A nearly linear evolution of two components of the deviator of the average second gradient rate of growth tensor is obtained, as shown in Fig. 9. Instead of looking at the evolution of individual components of the second gradient rate of growth tensor, we consider the condensed information provided by its first and second invariant in Fig. 10. We observe (Fig. 10) a nearly linear influence of the hydrostatic and deviatoric part of the hyperstress versus (traduced by the first and second invariants, respectively) the corresponding kinematic invariants. The isotropic and deviatoric parts of the average second gradient rate of growth tensor show quasi-linear evolutions versus the corresponding components of the average hyperstress tensor.

6 Identification of a strain gradient remodeling constitutive law for trabecular bone

We identify the six material parameters α, β, γ, δ, K, N of the constitutive model developed in Sect. 4 and summarized by the set of equations given in Box 2 by minimizing the mean square deviation between the components of the average first and second gradient of growth tensors $\left(\overline{\mathbf{D}}_{1g}\right)_{11}$, $\left(\overline{\mathbf{D}}_{1g}\right)_{22}$, $\left(\overline{\mathbf{D}}_{1g}\right)_{12}$, $\left(\overline{\mathbf{D}}_{2g}\right)_{111}$, $\left(\overline{\mathbf{D}}_{2g}\right)_{222}$,

Table 4 Set of material parameters for the identified second gradient constitutive law of growing bone

α	β	γ	δ	K (MPa)	N
−3.48E−4	2.57	−4.86E−9	1.36	1.09	1.58

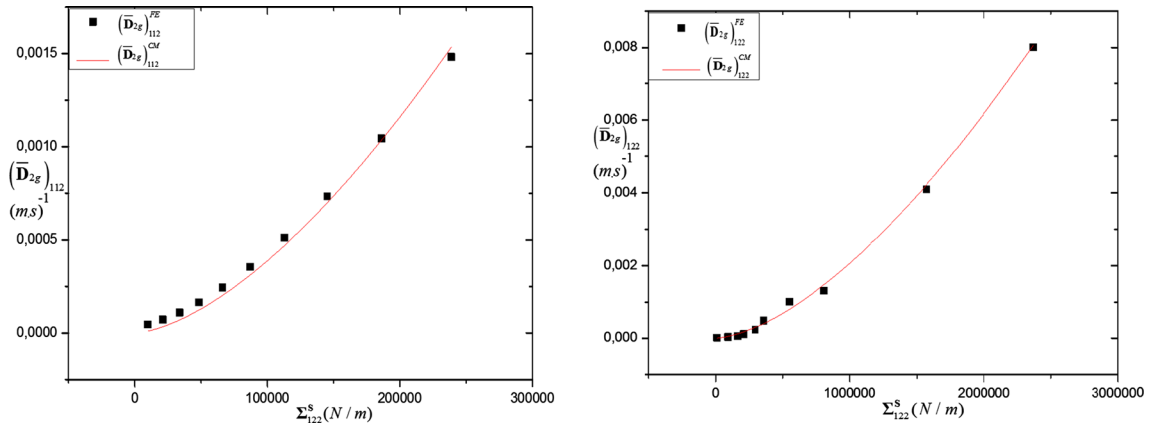

Fig. 11 Evolution of two components of the deviator $\left(\overline{\mathbf{D}}_{2g}\right)^D$ versus their counterpart for the driving hyperstress deviator $\left(\boldsymbol{\Sigma}^{\mathbf{S}} - \mathbf{X}_{2g}\right)^D$ predicted by the model and by direct FE simulations

$\left(\overline{\mathbf{D}}_{2g}\right)_{112}$, $\left(\overline{\mathbf{D}}_{2g}\right)_{212}$, $\left(\overline{\mathbf{D}}_{2g}\right)_{211}$, $\left(\overline{\mathbf{D}}_{2g}\right)_{122}$ predicted by the constitutive model—denoted $\left(\overline{\mathbf{D}}_{1g}\right)_{ij}^{CM}$, $\left(\overline{\mathbf{D}}_{2g}\right)_{ijk}^{CM} = \left(\overline{\mathbf{D}}_{2g}\right)_{ikj}^{CM}(\alpha, \beta, \gamma, \delta, K, N)$, $i, j, k = 1 \ldots 2$—and the same components evaluated by the FE simulations – denoted $\left(\overline{\mathbf{D}}_{1g}\right)_{ij}^{FE}$, $\left(\overline{\mathbf{D}}_{2g}\right)_{ijk}^{FE}$, $i, j, k = 1 \ldots 2$, so that we select the following function to be minimized over the searched parameters:

$$\underset{(\alpha,\beta,\gamma,\delta,K,N)}{Min} \sum_{k=1}^{Ntest} \left\{ \begin{array}{l} \left[\left(\overline{\mathbf{D}}_{1g}\right)_{11}^{FE} - \left(\overline{\mathbf{D}}_{1g}\right)_{11}^{CM}\right]^2 + \left[\left(\overline{\mathbf{D}}_{1g}\right)_{22}^{FE} - \left(\overline{\mathbf{D}}_{1g}\right)_{22}^{CM}\right]^2 + \left[\left(\overline{\mathbf{D}}_{1g}\right)_{12}^{FE} - \left(\overline{\mathbf{D}}_{1g}\right)_{12}^{CM}\right]^2 \\ + \left\{ \begin{array}{l} \left[\left(\overline{\mathbf{D}}_{2g}\right)_{111}^{FE} - \left(\overline{\mathbf{D}}_{2g}\right)_{111}^{CM}\right]^2 + \left[\left(\overline{\mathbf{D}}_{2g}\right)_{222}^{FE} - \left(\overline{\mathbf{D}}_{2g}\right)_{222}^{CM}\right]^2 + \left[\left(\overline{\mathbf{D}}_{2g}\right)_{112}^{FE} - \left(\overline{\mathbf{D}}_{2g}\right)_{112}^{CM}\right]^2 \\ \left[\left(\overline{\mathbf{D}}_{2g}\right)_{212}^{FE} - \left(\overline{\mathbf{D}}_{2g}\right)_{212}^{CM}\right]^2 + \left[\left(\overline{\mathbf{D}}_{2g}\right)_{211}^{FE} - \left(\overline{\mathbf{D}}_{2g}\right)_{211}^{CM}\right]^2 + \left[\left(\overline{\mathbf{D}}_{2g}\right)_{122}^{FE} - \left(\overline{\mathbf{D}}_{2g}\right)_{122}^{CM}\right]^2 \end{array} \right\} \end{array} \right\}_k$$

For each deformation mode (uniaxial tension along x and y, simple shear, and strain gradient components $k_{xxx}, k_{yyy}, k_{xxy}, k_{yxy}, k_{yxx}$, and k_{xyy}), five different tests corresponding to five stress and hyperstress levels are performed, so that previous functional is minimized over a total of $Ntest = 45$ tests. This leads to the identification of the following set of calibrated parameters indicated in Table 4.

The comparison of the evolution of the two components of the deviator $\left(\overline{\mathbf{D}}_{2g}\right)_{112}$ and $\left(\overline{\mathbf{D}}_{2g}\right)_{122}$ versus their counterpart for the driving hyperstress deviator predicted by the constitutive model and by direct FE simulations for a strain gradient loading (applied to the representative unit cell) combining $\left(\boldsymbol{\Sigma}^{\mathbf{S}} - \mathbf{X}_{2g}\right)_{122}^D$ and $\left(\boldsymbol{\Sigma}^{\mathbf{S}} - \mathbf{X}_{2g}\right)_{112}^D$ shows a very good agreement (Fig. 11). This highlights the capability of the identified second gradient growth model to predict the response of trabecular bone microstructures for general loadings at the scale of the representative unit cell.

7 Conclusion

Constitutive models for bone remodeling are constructed in the present contribution, based on micromechanical analyses at the scale of a representative volume element consisting of individual trabeculae defining the representative unit cell, accounting for both first- and second-order deformation gradients. On the microscale, trabeculae undergo apposition of new bone modeled by a surface growth velocity field driven by a mechanical stimulus identified to the surface divergence of an Eshelby-like tensor. The static and evolutive effective

properties of a periodic network of bone trabeculae are evaluated by combining a methodology for the evaluation of the average kinematic and static variables over a unit cell and numerical simulations with controlled imposed strain and strain gradient rates. The formulated effective growth constitutive law at the scale of the homogenized set of trabeculae (defining the mesoscopic level) relates the average first and second gradient growth strain rates to the homogenized stress and hyperstress tensors. The constitutive model is identified within the framework of the thermodynamics of irreversible processes, adopting a split of the kinematic and static tensors into their deviator and hydrostatic contributions based on the harmonic decomposition of the tensor space of third-order tensors.

The obtained evolutions of the first and second invariants of the average strain gradient rate of growth tensor versus similar invariants of the hyperstress tensor quantify the strength and importance of second gradient effects on the overall remodeling process. Numerical simulations further show that the marrow phase has a weak influence on the effective first and second gradient moduli (in comparison with the sole trabecular network in the absence of the marrow phase), and thus, it does weakly influence the overall remodeling process. The identified growth model accounting for strain gradient effects shall be used in zones where strain gradient effects are pronounced [16].

The formulated mesoscopic growth model shall prove useful for simulating bone sample microstructural evolutions at the macrolevel, with a good compromise between numerical efficiency and accuracy.

Appendix: Set of virtual tests designed for the determination of the effective first and second gradient effective moduli of the trabecular bone samples

The following first four tests are constructed to determine the first gradient stiffness tensor **C** as follows:

Uniaxial extension for C_{11}: When a uniform strain $\varepsilon_{xx} = 1$ (chosen as unity for simplicity) is applied on the unit cell's boundary, the displacement boundary conditions are

$$u_x = x,\ u_y = 0 \text{ on } \partial\Omega$$

This leads to identify C_{11} as

$$C_{11} = 2U_{RVE}/V_{RVR}$$

Uniaxial extension for C_{22}: When the uniform strain $\varepsilon_{yy} = 1$ is applied the unit cell's boundary, the displacement boundary conditions are

$$u_x = 0,\ u_y = y \text{ on } \partial\Omega$$

which gives

$$C_{22} = 2U_{RVE}/V_{RVE}$$

Biaxial extension for C_{12}: When the uniform strain $\varepsilon_{xx} = \varepsilon_{yy} = 1$ is applied on the unit cell's boundary, the displacement boundary conditions are

$$u_x = x,\ u_y = y \text{ on } \partial\Omega$$

which yields

$$C_{12} = \left(2U_{RVE}/V_{RVE} - C_{11} - C_{22}\right)/2$$

Shear deformation for C_{33}: When the uniform shear strain $\varepsilon_{xy} = 1$ is applied on the unit cell's boundary, the displacement boundary conditions are

$$u_x = y/2,\ u_y = x/2 \text{ on } \partial\Omega$$

which yields

$$C_{33} = 2U_{RVE}/V_{RVE}$$

We next evaluate the components of the second gradient stiffness tensor **D**; for this purpose, we perform the following six elementary tests:

For D_{111}: We apply the strain gradient component $k_{xxx} = \varepsilon_{xx,x} = u_{x,xx} = 1$ to the unit cell's boundary, and thus, the displacement boundary conditions are

$$u_x = x^2/2,\ u_y = 0 \text{ on } \partial\Omega$$

which gives

$$D_{111} = 2U_{RVE}/V_{RVE} - C_{11}x^2$$

For D_{222}: We apply the strain gradient component $k_{yyy} = \varepsilon_{yy,y} = \mathrm{u}_{y,yy} = 1$to the unit cell's boundary, and thus, the displacement boundary conditions are

$$u_x = 0,\ u_y = y^2/2 \text{ on } \partial\Omega$$

which gives

$$D_{222} = 2U_{RVE}/V_{RVE} - C_{22}y^2$$

For D_{112}: We apply the strain gradient component $k_{xxy} = \varepsilon_{xx,y} = \mathrm{u}_{x,xy} = 1$ to the unit cell's boundary, and thus, the corresponding boundary conditions are

$$u_x = xy,\ u_y = 0 \text{ on } \partial\Omega$$

which gives

$$D_{112} = 2U_{RVE}/V_{RVE} - C_{11}y^2$$

For D_{212}: We apply the strain gradient component $k_{yxy} = \varepsilon_{yy,x} = \mathrm{u}_{y,xy} = 1$ to the unit cell's boundary, and thus, the displacement boundary conditions are

$$u_x = 0,\ u_y = xy \text{ on } \partial\Omega$$

which gives

$$D_{212} = 2U_{RVE}/V_{RVE} - C_{22}x^2$$

For D_{211}: We apply the strain gradient component $k_{yxx} = \varepsilon_{xy,x} = 1/2\left(\mathrm{u}_{y,xx} + \mathrm{u}_{x,xy}\right) = 1$ to the unit cell's boundary, and thus, the displacement boundary conditions are

$$u_x = xy,\ u_y = x^2/2 \text{ on } \partial\Omega$$

which gives

$$D_{211} = 2U_{RVE}/V_{RVE} - C_{11}y^2$$

For D_{122}: We apply the strain gradient component $k_{xyy} = \varepsilon_{xy,y} = 1/2\left(\mathrm{u}_{y,xy} + \mathrm{u}_{x,yy}\right) = 1$ to the unit cell's boundary, and thus, the displacement boundary conditions are

$$u_x = y^2/2,\ u_y = xy \text{ on } \partial\Omega$$

which gives

$$D_{122} = 2U_{RVE}/V_{RVE} - C_{22}x^2$$

The derived second gradient elasticity tensor coefficients do in fact not depend on the choice the origin of the coordinate system with respect to the centroid of the tested RVE. When the origin of the coordinate axes is selected as the centroid of the tested RVE, the additional geometrical terms involving the coordinate do vanish.

References

1. Alibert, J.-J., Della Corte, A.: Second-gradient continua as homogenized limit of pantographic microstructured plates: a rigorous proof. Z. Angew. Math. Phys. **66**(5), 2855–2870 (2015)
2. Altenbach, H., Eremeyev, V.A.: On the linear theory of micropolar plates. ZAMM Z. Angew. Math. Mech. **89**(4), 242–256 (2009)
3. Berkache, K., Deogekar, S., Goda, I., Picu, R.C., Ganghoffer, J.-F.: Construction of second gradient continuum models for random fibrous networks and analysis of size effects. Compos. Struct. **181**, 347–357 (2017)
4. Bowman, S.M., et al.: Creep contributes to the fatigue behavior of bovine trabecular bone. J. Biomech. Eng. **120**, 647–654 (1998)
5. Buechner, P.M., Lakes, R.S.: Size effects in the elasticity and viscoelasticity of bone. Biomech. Model. Mechanobiol. **1**(4), 295–301 (2003)
6. Ciarletta, P., Preziosi, L., Maugin, G.A.: Mechanobiology of interfacial growth. J. Mech. Phys. Solids **61**, 852–872 (2013)
7. Cosserat, E., Cosserat, F.: Théorie des Corps Déformables. Librairie Scientifique A. Hermann et Fils, Paris (1909)
8. Cowin, S.C., Hegedus, D.H.: Bone remodeling I: theory of adaptive elasticity. J. Elast. **6**, 313–325 (1976)
9. dell'Isola, F., Seppecher, P., Della Corte, A.: The postulations á la D'Alembert and á la Cauchy for higher gradient continuum theories are equivalent: a review of existing results. Proc. R. Soc. Lond. Ser. A Math. Phys. Eng. Sci. **471**, 2183 (2015)
10. Epstein, M.: Kinetics of boundary growth. Mech. Res. Commun. **37**(5), 453–457 (2010)
11. Epstein, M., Maugin, G.A.: Thermomechanics of volumetric growth in uniform bodies. Int. J. Plast. **16**, 951–978 (2000)
12. Eringen, A.C., Edelen, D.G.B.: On nonlocal elasticity. Int. J. Eng. Sci. **10**(3), 233–248 (1972)
13. Fernandes, P.R., Folgadoa, J., Jacobs, C., Pellegrini, V.: A contact model with ingrowth control for bone remodelling around cementless stems. J. Biomech. **35**, 167–176 (2002)
14. Field, C., Li, Q., Li, W., Thompson, M., Swain, M.: A comparative mechanical and bone remodelling study of all-ceramic posterior inlay and onlay fixed partial dentures. J. Dent. **40**(1), 48–56 (2012). https://doi.org/10.1016/j.jdent.2011.10.003
15. Frasca, P., Harper, R., Katz, J.L.: Strain and frequency dependence of shear storage modulus for human single osteons and cortical bone microsamples-size and hydration effects. J. Biomech. **14**(10), 679–690 (1981)
16. Ganghoffer, J.F., Sokolowski, J.: A micromechanical approach to volumetric and surface growth in the framework of shape optimization. Int. J. Eng. Sci. **74**, 207–226 (2014)
17. Ganghoffer, J.F.: Mechanical modeling of growth considering domain variation-part II: volumetric and surface growth involving Eshelby tensors. J. Mech. Phys. Solids **58**(9), 1434–1459 (2010)
18. Ganghoffer, J.F.: A contribution to the mechanics and thermodynamics of surface growth, application to bone remodeling. Int. J. Eng. Sci. **50**(1), 166–191 (2012)
19. Ganghoffer, J.F., Plotnikov, P.I., Sokolowski, J.: Mathematical modeling of volumetric material growth. Arch. Appl. Mech. **84**(9–11), 1357–1371 (2014)
20. Giorgio, I., Andreaus, U., dell'Isola, I., Lekszycki, T.: Viscous second gradient porous materials for bones reconstructed with bio-resorbable grafts. Extreme Mech. Lett. **13**, 141–147 (2017)
21. Goda, I., Assidi, M., Belouettar, S., Ganghoffer, J.-F.: A micropolar anisotropic constitutive model of cancellous bone from discrete homogenization. J. Mech. Behav. Biomed. Mater. **16**, 87–108 (2012)
22. Goda, I., Assidi, M., Ganghoffer, J.-F.: A 3D elastic micropolar model of vertebral trabecular bone from lattice homogenization of the bone microstructure. Biomech. Model. Mechanobiol. **13**, 53–83 (2014)
23. Goda, I., Ganghoffer, J.-F.: 3D plastic collapse and brittle fracture surface models of trabecular bone from asymptotic homogenization method. Int. J. Eng. Sci. **87**(58–82), 2015 (2015b)
24. Goda, I., Ganghoffer, J.-F.: Construction of first and second order grade anisotropic continuum media for 3D porous and textile composite structures. Compos. Struct. **141**, 292–327 (2016)
25. Goda, I., Ganghoffer, J.F., Maurice, G.: Combined bone internal and external remodeling based on Eshelby stress. Int. J. Solids Struct. **94–95**, 138–157 (2016a)
26. Goda, I., Ganghoffer, J.-F.: Identification of couple-stress moduli of vertebral trabecular bone based on the 3D internal architectures. J. Mech. Behav. Biomed. Mater. **51**, 99–118 (2015a)
27. Goda, I., Rahouadj, R., Ganghoffer, J.-F.: Size dependent static and dynamic behavior of trabecular bone based on micromechanical models of the trabecular. Int. J. Eng. Sci. **72**, 53–77 (2013)
28. Goda, I., Rahouadj, R., Ganghoffer, J.-F., Kerdjoudj, H., Siad, L.: 3D couple-stress moduli of porous polymeric biomaterials using μCT image stack and FE characterization. Int. J. Eng. Sci. **100**, 25–44 (2016b)
29. Harrigan, T.P., Jasty, M.J., Mann, R.W., Harris, W.H.: Limitations of the continuum assumption in cancellous bone. J. Biomech. **21**, 269–275 (1988)
30. Kröner, E.: Elasticity theory of materials with long range cohesive forces. Int. J. Solids Struct. **3**(5), 731–742 (1976)
31. Lacroix, D., Prendergast, P.J.: A mechano-regulation model for tissue differentiation during fracture healing: analysis of gap size and loading. J. Biomech. **35**, 1163–1171 (2002)
32. Lakes, R.: Experimental methods for study of Cosserat elastic solids and other generalized elastic continua. In: Muhlhaus, H.-B. (ed.) Continuum Models for Materials with Microstructure, pp. 1–22. Wiley, New York (1995)
33. Lemaitre, J., Chaboche, J.L.: Mécanique des matériaux solides. Dunod, Paris (2009)
34. Louna, Z., Goda, I., Ganghoffer, J.F., Benhadid, S.: Formulation of an effective growth response of trabecular bone based on micromechanical analyses at the trabecular level. Arch. Appl. Mech. **87**(3), 457–477 (2016)
35. Louna, Z., Goda, I., Ganghoffer, J.F.: Identification of a constitutive law for trabecular bone samples under remodeling in the framework of irreversible thermodynamics. Thermodyn. Contin. Mech. (2018). https://doi.org/10.1007/s00161-018-0619-9
36. Madeo, A., George, D., Lekszycki, T., Nierenberger, M., Rémond, Y.: A second gradient continuum model accounting for some effects of micro-structure on reconstructed bone remodeling. C. R. Méc. **340**(8), 575–589 (2012)
37. Madeo, A., Lekszycki, T., dell'Isola, F.: Continuum model for the bio-mechanical interactions between living tissue and bio-resorbable graft after bone reconstructive surgery. C. R. Méc. **339**(10), 625–682 (2011)

38. Maire, E., Withers, P.J.: Quantitative X-ray tomography. Int. Mater. Rev. **59**, 1–43 (2014)
39. McNamara, L.M., Prendergast, P.J.: Bone remodelling algorithms incorporating both strain and microdamage stimuli. J. Biomech. **40**, 1381–1391 (2007)
40. Olivares, L., Lacroix, D.: Computational methods in the modeling of scaffolds for tissue engineering. In: Geris, L. (ed.) Computational Modeling in Tissue Engineering, pp. 107–126. Springer, Berlin (2013)
41. Olive, M., Auffray, N.: Isotropic invariants of a completely symmetric third-order tensor. J. Math. Phys. American Institute of Physics (AIP) **55**(9), 1.4895466 (2014)
42. Park, H.C., Lakes, R.S.: Cosserat micromechanics of human bone: strain redistribution by a hydration sensitive constituent. J. Biomech. **19**(5), 385–397 (1986)
43. Ramézani, H., El-Hraiech, A., Jeong, J., Benhamou, C.-L.: Size effect method application for modeling of human cancellous bone using geometrically exact Cosserat elasticity. Comput. Methods Appl. Mech. Eng. **237**, 227–243 (2012)
44. Reda, H., Goda, I., Ganghoffer, J.F., L'Hostis, G., Lakiss, H.: Dynamical analysis of homogenized second gradient anisotropic media for textile composite structures and analysis of size effects. Compos. Struct. **161**, 540–551 (2017)
45. Sanz-Herrera, J., Garcia-Aznar, J., Doblaré, M.: On scaffold designing for bone regeneration: a computational multiscale approach. Acta Biomater. **5**(1), 219–229 (2009)
46. Skalak, R., Farrow, D.A., Hoger, A.: Kinematics of surface growth. J. Math. Biol. **35**, 869–907 (1997)
47. Taylor, M., Cotton, J., Zioupos, P.: Finite element simulation of the fatigue behaviour of cancellous bone. Meccanica **37**, 419–429 (2002)
48. Wagner, D.W., Lindsey, D.P., Beaupre, G.S.: Deriving tissue density and elastic modulus from microCT bone scans. Bone **49**(5), 931–938 (2011)
49. Wang, C., Han, J., Li, Q., Wang, L., Fan, Y.: Simulation of bone remodelling in orthodontic treatment. Comput. Methods Biomech. Biomed. Eng. **17**(9), 1042–1050 (2012)
50. Yang, J.F.C., Lakes, R.S.: Transient study of couple stress effects in compact bone: Torsion. J. Biomech. Eng. **103**, 275–279 (1981)
51. Yang, J.F.C., Lakes, R.S.: Experimental study of micropolar and couple stress elasticity in compact bone in bending. J. Biomech. **15**(2), 91–98 (1982)